Preface

This is the Master's thesis of my Master of Science degree in Applied Physics and Mathematics. The work on this project was done from November 2018 to April 2019 at The Laboratory for Soft and Complex Matter Studies at NTNU. I would like to thank my supervisor Professor Jon Otto Fossum at the Department of Physics at NTNU for his help and guidance, Staff Engineer Ole Tore Buset, for his help and patience, Øystein Gjervan Hagemo and the fine mechanical workshop at the NV faculty for their help and Konstanse Seljelid for her helpful insights and assistance with the experiments. I also in particular want to thank Co-supervisor and friend, Kristoffer Hunvik for his help and guidance.

Vegard Josvanger
April 2019
Trondheim

Abstract

Smectite is a type of clay mineral which, due to its slight negative layer charge and charge compensating interlayer cations, has the ability to adsorb carbon dioxide. It has a large adsorption capability and is abundant in caprock which makes it ideal for Carbon Capture Storage in empty gas and oil fields. CO_2 adsorption in smectite is dependent on interlayer cation, pressure, humidity and temperature and can be measured with X-ray diffraction.

In order to preform such X-ray diffraction measurements at a X-ray home station an experimental setup had to be designed and created. Giving in-situ control of temperature and pressure on the clay sample.

The experimental setup presented has the ability of preforming in-situ X-ray diffraction measurements on clay powder with temperature control between 253 and 400 Kelvin and pressure control between 0 and at least 40 bars.

Sammendrag

Smektitt er en type leire som på grunn av sin svakt negative lag-ladning og ladningskompenserende kation, har evnen til å adsorbere karbondioksid. Leiren har stor adsorbsjonskapasitet og finnes rikelig mengder i takbergarter noe som gjør den ideel for karbonfangst og lagring i tomme oljereservoar. Adsorbasjon av karbondioksid i smektitt er avhengig av temperatur, trykk, fuktighet og mellomlags kation og kan undersøkes med røntgendiffraksjon.

For å gjennom føre røntgendiffraksjons forsøk på hjemmelaboratoriet må et eksperimentelt oppsett utformes. Oppsettet gir in-situ kontroll over både trykk og temperatur til leireprøven.

Det eksperimentelle oppsettet presentert her kan gjøre in-situ røntgendiffraksjons målinger med temperatur kontroll mellom 253 og 400 Kelvin, og trykkontroll mellom 0 og i det minste 40 bar.

Table of Contents

List of Tables

List of Figures

Chapter 1

Introduction

1.1 Motivation and Background

1.1.1 Climate Change

On October 8th 2018 The Special Report on Global Warming of 1.5 °C(SR15) was released by the Intergovernmental Panel on Climate Change(IPCC). The report presented the panels findings on the purported effects of increased global temperature, the mediation of limiting the increase to 1.5 °C, as opposed to 2 °C and a way to meet this limited increase of global temperature.

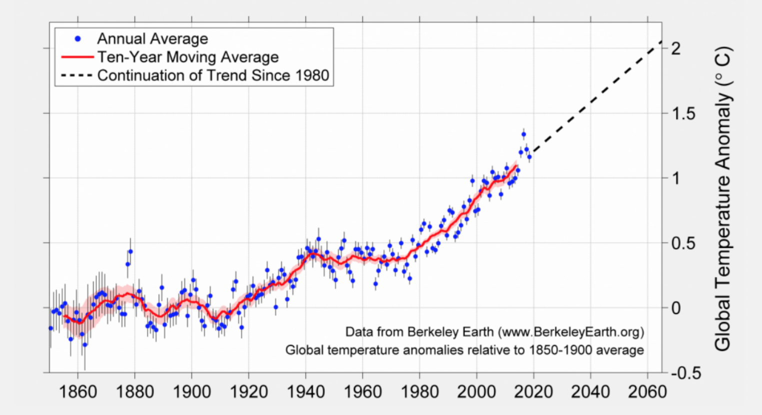

Figure 1.1: Global temperature anomaly relative to the average temperature from 1850 to 1900 with projected trend. Figure from [4].

According to the IPCC, a body of the United Nations, the global average temperature on earth has increased 1 °C from the Industrial Age until today and at the current rate of climate gas emission the temperature is projected to reach 1.5 °C sometime between 2030 and 2050 [27]. Projected trend in temperature from Berkley Earth[4] can be seen in figure 1.1. In addition the increased temperature of water and air, this will also cause higher sea levels and more extreme weather. Which poses an increased risk to ecosystems, human livelihood, food production, water security and economic growth. SR15 stated that these effects would be even more severe at an increase of 2 °C.

In order to limit the increase in global temperature to 1.5 °C it is necessary to reduce human emissions by 45% from 2010 levels. To achieve this a wide variety of emission cuts and mitigation measures must be implemented. Transitions in energy, land, infrastructure and industrial systems are needed to bring about a deep emission cuts. This includes conversion of pasture land to land for food or energy crops, more energy effective uses of carbon emitting fuels and a higher dependence on low emission fuels. The report also stated that emissions can be counteracted through carbon dioxide removal and mitigated through Carbon Capture and Storage.

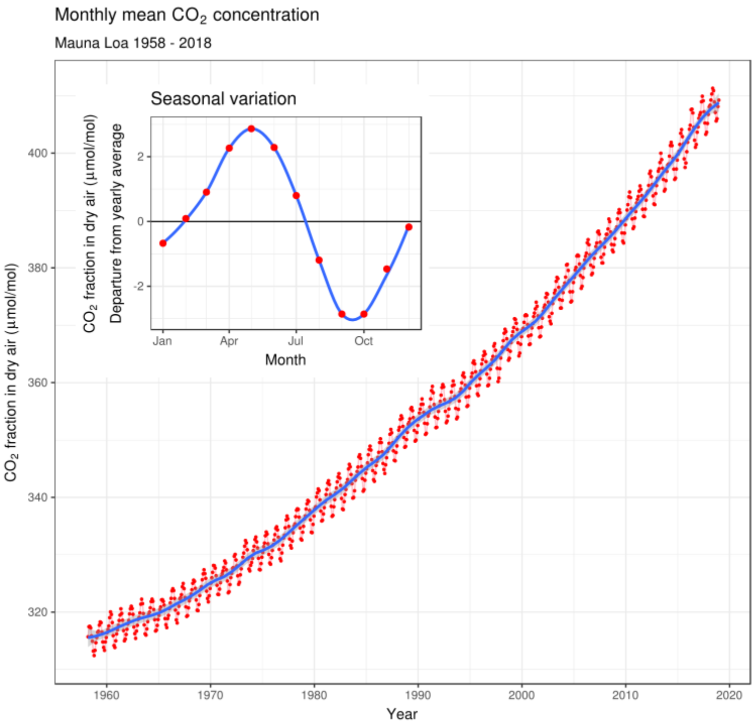

Data : R. F. Keeling, S. J. Walker, S. C. Piper and A. F. Bollenbacher
Scripps CO2 Program (http://scrippsco2.ucsd.edu). Accessed 2019-01-06

Figure 1.2: How the CO_2 in the atmosphere has increased over time. Figure courtesy Dr. Pieter Tans, NOAA/ESRL and Dr. Ralph Keeling, Scripps Institution of Oceanography. Updated figure first published in 2005 [38].

1.1.2 Carbon Capture and Storage

Carbon Capture and Storage(CCS) is a process wherein carbon dioxide is separated from other industrial emissions and captured at industry or energy-related sources for it to be compressed and stored long term. Currently the potential storage methods most considered are geological storage, ocean storage and industrial fixation of CO_2 in inorganic carbonates [42]. Geological storage of CO_2 is mainly done by injection into saline formations at oil or gas fields at a depth of about 800m. Here the main criteria for trapping would be the existence of caprock i.e "rock of very low permeability that acts as an upper seal to prevent fluid flow out of a reservoir" [42]. Most caprock are composed of clay, often illite, kaolinite, chlorite or smectite. With the main trapping mechanisms of structural and residual trapping[8]. Structural trapping is a continuous column of CO_2 trapped under a sealing caprock. The pressure from the column must be balanced by the capillary entry pressure from the seal. Residual trapping are disconnected gas bubbles confined in caprock pores. Inside the caprock the CO_2 interacts with the nanopores in the clay and is adsorbed on the surface [8]. The latter trapping mechanism could also be used to capture carbon dioxide at land and further study of this adsorption could lead to more effective clay based CCS technology and hopefully mitigate the upcoming climate crisis.

Even though geological storage of CO_2 mainly concerns pumping the gas down into empty gas and oil fields and saline formations, clay material can also be used in carbon capture at the point source of pollution at close to ambient conditions, for it to then be buried. Either way it is a point of interest for further scientific investigation. Clay is ideal for CCS because of its availability, its environmental friendliness, non-toxicity and has a low level of greenhouse gas emission during processing. In addition to this it is stable, has low production cost and large CO_2 storage capacity [30].

In order to better understand the interaction between CO_2 and the clay minerals at subsurface conditions several studies have been done. In connection to this several studies on smectite has been done at the Laboratory for Soft and Complex Matter Studies at the Department of Physics at the Norwegian University of Science and Technology(NTNU). This master thesis is a part of their work with the expressed goal of designing and building an experimental setup for their home X-ray station.

It has been discovered that smectite is capable of adsorbing and retain large amounts of CO_2[30]. This capability has been shown to be pressure, temperature and interlayer cation dependent. In order to study this adsorption a setup is designed to be able to preform in-situ X-ray diffraction experiments at a wide range of temperatures, from 253 K to 423 K, and exposed to CO_2 at a range of pressure conditions.

1.2 Structure of the report

The outline of the report will be as follows. In chapter 2 the basic theory behind clay and intercalation will be presented. As well as a theoretical background for the experimental technique and temperature control. Chapter 3 will give a detailed description of the experimental equipment and setup, as well as description of three experiments preformed using said equipment and setup. In chapter 4 the results from the experiments as well as procedures integral to the accuracy of the measurements will be presented. Followed by a discussion in chapter 5 of the results and possible further development. Ultimately a conclusion will be drawn in chapter 6.

Chapter 2

Theory

In this section a brief introduction to the material in question will be presented. Important aspects of clay, specifically smectite and fluorohectorite and their interaction with water and carbon dioxide. A theoretical background for the technique used to examine the adsorption in smectite and the control process for the temperature control.

2.1 Clay

2.1.1 General on clay.

There is no all encompassing definition of clay which is acceptable to all disciplines[19], it is however necessary to establish a working definition when investigating the properties of clay and even more when discussing one particular type. For that reason the following is what is meant by clay minerals in this text.

Clay minerals are in general composed of hydrous phyllosilicates, a silicon oxygen compound, with a sheetlike structure and small particle size. They can also contain significant amounts of iron, alkali metals, or alkaline earths. These minerals can either be synthetic or natural[18, 19]. Phyllosilicates, which makes up fine-grained fractions of rocks, sediments and soil, are categorized by their layer structure, anisotropy of particles, planar, edge and interlayer surfaces, plasticity and hardening on drying or firing. The internal and external surfaces can also easily be modified by adsorption, ion exchange and grafting [19].

The phyllosilicates, sheet silicates, are based on two types of layers. The 1:1 layer where one tetrahedral sheet is bonded to an octahedral sheet, or the 2:1 layer where one octahedral sheet is sandwiched between two tetrahedral sheets. The tetrahedral sheet consists of an oxygen atom in each corner of a tetrahedron surrounding a cation. This cation is commonly either a silicon, aluminum or an iron ion [19, 33]. The tetrahedrons are linked at the three basal oxygen atoms in the a,b-plane and forms a two dimensional hexagonal sheet in this plane. For reference the figure 2.1 is the a,c-plane. The last oxygen atom in the apical

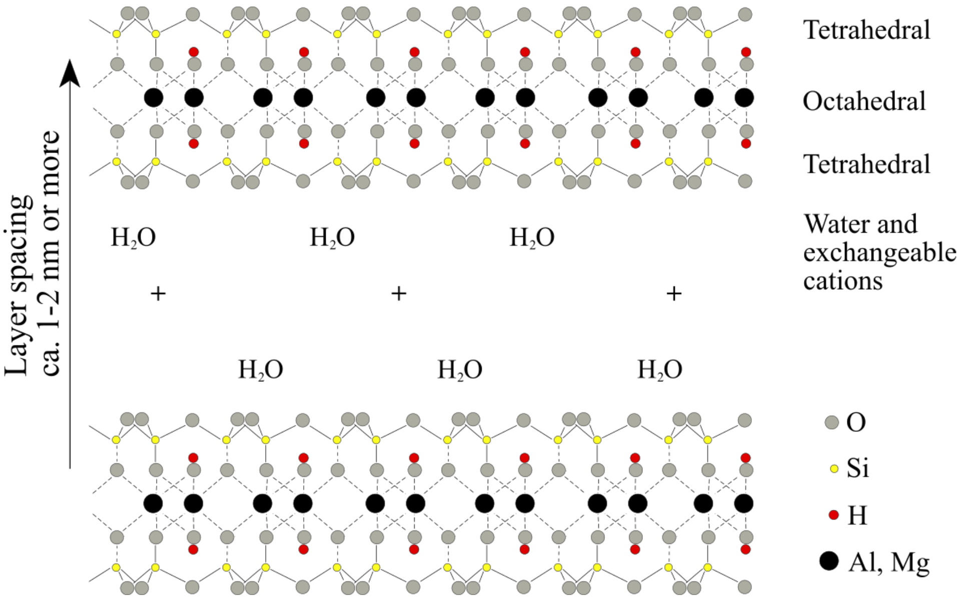

Figure 2.1: Illustration of two smectite 2:1 layer where a octahedral layer is sandwiched between two tetrahedral layers. Between the layers there are cations and water molecules. Modified figure originally from [44].

position is shared to form an octahedral sheet where a cation is surrounded by shared oxygen atoms or an unshared hydroxy group at the corners of an octahedron. The cation is commonly a Li, Mg, Fe or Al ion[18, 19]. Common types of 1:1 silicate layer clays are Kaolin and Serpentine. In a 2:1 layer a tetrahedral silicate sheet is oriented in the opposite direction to the first and attached on the other side of the octahedral sheet [18]. These layers can be of one single unit layer, as seen in figure 2.1, or stacked with several layers depending on environmental conditions. The clay layers are either electrically neutral or have a net negative charge due to isomorphic substitutions[19]. Common types of 2:1 silicate layer clays are pyrophyllite, talc, mica and smectite. Where pyrophyllite and talc have electricaly neutral layers which are held together by Van der Waals bonding. While mica and smectite have slightly negative layer charge. This negative layer charge is an important quality of the 2:1 phylosilicates since it induces occupancy in the interlayer by exchangeble charge-compensating-cations such as Li^+, Na^+ and Ni^{2+}[33, 19].

2.1.2 Smectite and Fluorohectorite

Smectite has silicate layers of the 2:1 type, particles of colloidal size, high surface area, high degree of stacking disorder and a moderate layer charge. It also features considerable interlayer swelling. This happens among other when foreign molecules such as H_2O and CO_2 enters the interlayer space between the silicate sheets. This is also called intercalation[33, 19].

Since impurities in natural clay may mask some of their physical and chemical properties synthetic clays are used in there stead. Fluorohectorites (Fh) are synthetic smectites which are found to be a representative and clean model for natural smectite clays. The nominal chemical formula per unit cell is:

$$\mathrm{M_x(Mg_{6\text{-}x}Li_x)Si_8O_{20}F_4} \tag{2.1}$$

[33, 21, 30]. Where M represent an interlayer cation, either Na^+, Li^+or Ni^{2+}. Substitution of Mg^{2+} with Li^+ in the octahedral sheet gives a negative layer charge. Fluorohectorite, as a form of smectite, is a 2:1 phyllosilicate with a layer distance of approximately 1nm [30]. Since Li^+ substitutes for Mg^{2+} in the octahedral sheet sites, it is classified as a tri-octahedral smectite. Fluorohectorite differentiates itself from hectorite by having fluorine at the apex of its tetrahedral structure, as opposed to hectorite which has OH groups their instead. It comes in a range of particle sizes from nanometers up to $10\mu m$ [21].

The interlayer cations can be switched with others through cation exchange. This is a process wherein the cations balancing the negative layer charge are exchanged with other cations in a solution. This is reversible and there is selectivity of cations. The cation exchange is implemented by mixing the clay in a salt solution of approximately 0.5-1 M. for 24 hours. Followed by centrifuge and further suspension in the solution to remove the remaining surplus of exchangeable cations [21].

2.1.3 Intercalation of Water

The most common molecule clay minerals interacts with is water. This interaction happens every place there exists naturally occurring moisture. Here we concern ourselves with the intercalation of H_2O molecules in smectite. The swelling, caused by the intercalation, is controlled by negative charges of the layers and the interlayer cations. The repeating distance between the layers, the basal-spacing, is dependent on the amount of intercalated molecules, and increases during swelling. The basal spacing is also referred to as the d-spacing. Some amount of water intercalation is energetically more favorable then others. Therefore certain discrete d-spacings are common and will be denoted in terms of water layers. xWL, for $x = 1, 2$ or 3. The distance is mainly dependent on the environmental conditions relative humidity and temperature and is in general measured using X-ray diffraction [33, 19, 23]. Experiments have shown that the clay can be completly dehydrated by heating at 423K for a couple of minutes or at 343K for several hours under vacuum. Here the clay ended up with a basal distance of 1.14 nm for NiFh with $x = 0.6$ in (2.1). [23].

2.1.4 Intercalation of Carbon Dioxide

Intercalation of carbon dioxide in clay is a relatively recent area of scientific study and is still not well understood [24, 36], yet several studies shows that it is possible to intercalate and retain CO_2 in Smectite [43, 36, 24, 30, 22]. These studies have shown that the intercalation is highly dependent on the interlayer cation, temperature and pressure. Where the ionic radius of the cation have been found to affect the interlayer separation when it is

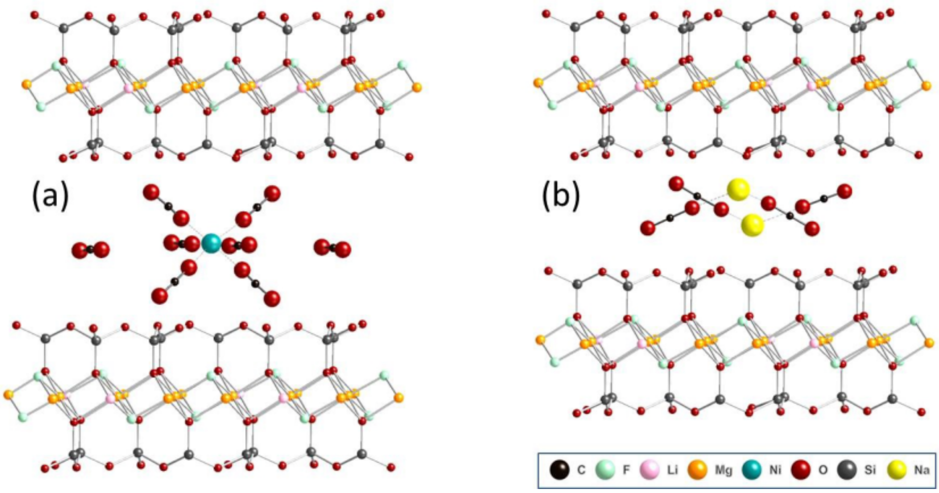

Figure 2.2: Suggestion of how CO_2 is intercalated in fluorhectorite. Figures originally from "A nano-silicate material with exceptional capacity for co2 capture and storage at room temper-ature" [30] where it was made with the program CrystalMaker®. Figure courtesy of Leide Cavalcanti.

occupied by CO_2. Larger radius corresponds with larger separation [30]. The intercalation is measured among other techniques with X-ray diffraction and volumetric absorption. An illustration of how CO_2 could possibly occupy the interlayer space in smectite can be seen in figure 2.2.

To describe the sorption kinetics of carbon dioxide adsorption the Arrhenius equation can be used [23], and is given by

$$\frac{dn}{dt} = n_0 \frac{1}{\tau} f\left(\frac{n}{n_0}\right) \tag{2.2}$$

Where n is the amount of adsorbed molecules on the surface and $\frac{1}{\tau}$ is the rate constant, which is dependent on temperature and pressure. n_0 is the total number of molecules available. What type of equation $f\left(\frac{n}{n_0}\right)$ is depends on the which type of adsorption mechanism is acting. For a first order adsorption process, where the adsorbed molecules statistically occupy one adsorption site, the equation becomes

$$f\left(\frac{n}{n_0}\right) = 1 - \frac{n}{n_0} \tag{2.3}$$

Combining the equations (2.2) and (2.3)

$$\frac{dn}{dt} = n_0 \frac{1}{\tau}\left(1 - \frac{n}{n_0}\right) \tag{2.4}$$

$\frac{n}{n_0}$ is proportional to the normalized X-ray intensity(NI). Integrating the equation for adsorbed molecules becomes

$$n(t) = n_0(1 - e^{-t/\tau}) \tag{2.5}$$

And the intensity becomes:

$$NI = 1 - e^{-t/\tau} \tag{2.6}$$

2.2 X-rays

X-rays are electromagnetic waves with wavelengths generally between $1 \cdot 10^{-3}$ nm and 10 nm [17]. This corresponds to photons with energy between 1240 keV and 124 eV, given through the numerical relation between energy and wavelength [1]

$$\lambda[\text{Å}] = \frac{hc}{E} = \frac{12.398}{\text{photon energy[keV]}} \tag{2.7}$$

Where λ is the wavelength, c is the speed of light and h is plank's constant. An electromagnetic wave, when propagating along a direction **k** has an electric field, **E**, perpendicular to the direction and a magnetic field **H** perpendicular to both **k** and **E** [1]. Where the electric field at point **r** and at time, t, polarized in the direction of the unit vector $\hat{\epsilon}$, can be expressed as

$$\mathbf{E}(\mathbf{r}, t) = \hat{\epsilon} E_0 e^{i(\mathbf{k} \cdot \mathbf{r} - \omega t)} \tag{2.8}$$

Here the angular wavenumber $k = 2\pi/\lambda$ is the spacial frequency and ω is the temporal angular frequency of the wave, while E_0 is magnitude of the electric field.

This wave can also be described through quantum mechanics, where the wave is quantized into photons with energy $\hbar\omega$ and momentum $\hbar\mathbf{k}$, where $\hbar$ is the reduced Planck constant $(h/2\pi)$. The intensity of the X-ray beam is given by the number of photon passing through an area per second and is proportional to the square of the electric field[1].

2.2.1 X-ray Generation

X-ray photons can be produced through electron acceleration or excitation. Here we will focus on the latter. Electrons emitted form a hot filament may be accelerated in a high voltage potential cathode-anode tube under vacuum. The accelerated electron releases its kinetic energy upon collision with the anode. Some of this energy is converted to electromagnetic radiation i the X-ray regime. This happens through two processes. Either by photoelectric excitation and subsequent emission of photons from the atoms in the anode, or by electromagnetic interaction with the Coulomb field of the anode[1, 35].

The exited electrons at the anode emit photos with characteristic energies during relaxation. For the emitted photons to have energy in the X-ray regime, ionization of the core level electrons is needed. The most prominent lines in the emission spectrum are from the energy states L and M to the innermost K state [1, 35]. The peak in intensity from these transitions, in a X-ray spectrum, are labeled K_α and K_β respectively. These characteristic peaks can be seen in figure 2.3 where $K_{\alpha I-II}$ is the large peak and K_β is the smaller one.

The second way impinging electrons may produce X-rays is through the loss of their kinetic energy when interacting with the anodes coulomb field. In this process the electrons

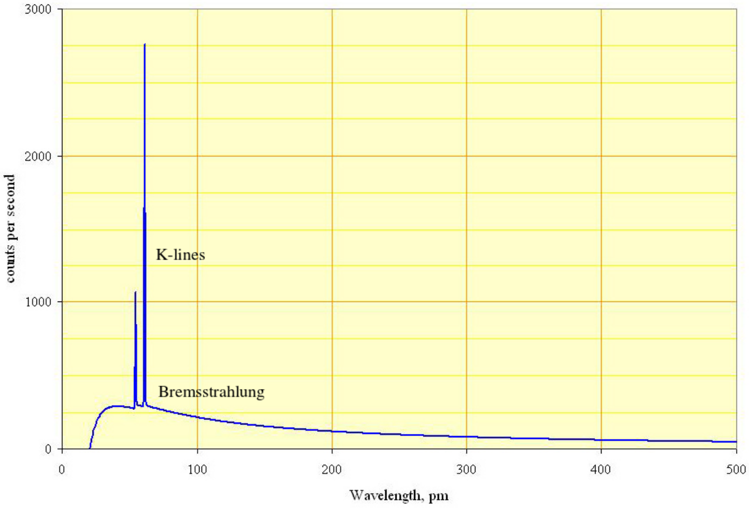

Figure 2.3: Typical spectrum for a Rhodium-Target X-ray tube at 60 keV. Here the characteristic peaks for Rh are $K_{\alpha I-II}$ and $K_{\beta I}$. The $K_{\alpha I}$ peak has an energy of 20.2161 keV and $K_{\alpha I}$ has of 20.0737 keV, corresponding to to a wavelength of 61.3 pm and 61.8 pm, which are indistinguishable in the figure and therefor collected to one high line. While the shorter line is for $K_{\beta 1}$ with an energy of 22723.6 keV corresponding to the wavelength 54.6 pm. Modified figure originally from [31]

kinetic energy is converted into radiation through a series of collisions. Resulting in the emission of a continuous spectrum, called Bremsstrahlung. This specter has an upper energy limit equal to the entire kinetic energy of the electron. This is from the cases were the entire kinetic energy of the electron is converted into one photon. A X-ray spectrum can be seen in figure 2.3 with two clear peaks and Bremsstralung at the base of the intensity plot.

X-rays interact with matter either through absorption or scattering [1].

2.2.2 X-ray Absorption

X-rays have the ability to penetrate different materials. This ability is energy and material dependent. A beam of mono-energetic X-rays with incident intensity I_0 will emerge with an intensity given by:

$$I(x) = I_0 \, e^{-\mu \, x} \tag{2.9}$$

after penetrating a material of mass thickness x. μ is the linear attenuation coefficient for a homogeneous material. This is called Beer-Lambert's law [1].

2.2.3 Scattering

Classical description of X-ray scattering is that the incident X-ray exert a force on the electric charge of the target. The electric charge is then accelerated and radiates the scattered wave. The scattered wave has the same wavelength, therefore also energy, as the incident wave. The scattering is therefore elastic. Elastic scattering of photons is also known as Thompson scattering. Inelastic scattering, also known as Compton scattering, is when the scattered wave has longer wavelength than the incident wave and therefore lower energy. In order to explain this a quantum mechanical approach is necessary. Here the photon has the energy $\hbar\omega$ and momentum $\hbar\mathbf{k}$ and the photon transfers some of its energy to the interaction electron and is scattered with a longer wavelength [1, 17]. Since the main interaction in X-ray diffraction is elastic scattering the classical approach is used in this case.

The scattering of an electron is given through the differential scattering cross-section[1]

$$\left(\frac{d\sigma}{d\Omega}\right) = \frac{I_{sc}}{\Phi_0 \Delta\Omega} \tag{2.10}$$

Where the incident beam is given through the flux, Φ_0, which is the number of photons passing through an unit area per second. I_{sc} is the number of scattered photons per second recorded at a detector at position R from the electron, and subtends a solid angle $\Delta\Omega$. The scattered intensity is proportional to the energy density of the radiated electric field, $|\mathbf{E}_{rad}|^2$. Therefore the number density of the scattered photons is proportional to $|\mathbf{E}_{rad}|^2/\hbar\omega$. This times the speed of light, c, and the area of the detector, $R^2\Delta\Omega$, gives the an expression for the scattered intensity

$$I_{sc} \propto c(R^2\Delta\Omega)|\mathbf{E}_{rad}|^2/\hbar\omega \tag{2.11}$$

2.2.4 X-ray Diffraction(XRD)

The scattering of X-ray beams can be described in terms of the phase difference between incident and scattered wave, as in (2.8), with wavevector **k** and the scattered wave with wavevector **k'**. This difference, called the scattering vector can be seen in figure 2.4 and is given by:

$$\mathbf{q} = \mathbf{k} - \mathbf{k'} \tag{2.12}$$

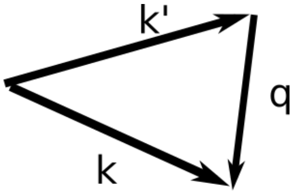

Figure 2.4: Relationship between incident wavevector k, scattered wavevector k' and scattering vector q

For constructive interference between waves scattered from a sample, the scattering vector **q** times the distance, **r**, needs to be equal to a integer multiple of 2π. More on this later.

Considering the scattering from an atom with Z electrons. Here the electron density is given by $\rho(\mathbf{r})$ and the scattered wave can the be described according to the atoms form factor. The atomic form factor, the measure of the scattering amplitude of a wave from a single atom, is

$$f(\mathbf{q}) = \int \rho(\mathbf{r}) e^{i\mathbf{q}\cdot\mathbf{r}} d\mathbf{r} \tag{2.13}$$

Where the exponential part is the phase factor. The atomic form factor goes to Z, the number of electrons in the atom, at the limit $q \rightarrow 0$ and 0 when $q \rightarrow \infty$. All electrons scatter in phase versus all electrons scatter out of phase.

Scattering from a molecule or a unit cell which is smallest group of repeating atoms in a crystal, is given in similar terms as the atomic form factor

$$F(\mathbf{q}) = \sum_j f_j(\mathbf{q}) e^{i\mathbf{q}\cdot\mathbf{r}_j} \tag{2.14}$$

This sum is the contribution from the atoms, $f_j(\mathbf{q})$, times the phase factor $e^{i\mathbf{q}\cdot\mathbf{r}_j}$.
Taking this a step further it can be applied to the scattering from a crystal, or any large arrangement with repeating structure, as:

$$S(\mathbf{q}) = \sum_j f_j(\mathbf{q}) e^{i\mathbf{q}\cdot\mathbf{r}_j} \sum_n e^{i\mathbf{q}\cdot\mathbf{R}_n} \tag{2.15}$$

Here the amplitude of the crystal scattering is given by the multiplication of the unit cell form factor with the sum of the phase factor for every other lattice point, which is the sum over lattice sites in a crystal or sheets in clay. The structure factor is one of the factors determining the intensity of the diffracted X-rays.

In crystallography the scattering vector must be a reciprocal lattice vector for constructive interference to occur. While smectite is not a crystal it does however have small scale stacking order of layers and some terms and theory from crystallography is useful to describe the diffraction. The crystal translation vector, $\mathbf{R}_n$, is given by:

$$\mathbf{R}_n = n_1\mathbf{a}_1 + n_2\mathbf{a}_2 + n_3\mathbf{a}_3 \tag{2.16}$$

Where n_1, n_2, n_3 are integers and $\mathbf{a}_1, \mathbf{a}_2, \mathbf{a}_3$ are the primitive lattice vectors for the crystal. After translation along $\mathbf{R}_n$, with arbitrary n values, the crystal looks the same as before the translation [29]. In the case of clay this is only possible on a short scale. From one two dimensional layer, spanned by $\mathbf{a}_1$ and $\mathbf{a}_2$, to another layer along vector $\mathbf{a}_3$.
Here it becomes necessary to introduce the concept of the reciprocal lattice. This is a lattice spanned by the reciprocal lattice basis vectors:

$$\mathbf{b}_1 = 2\pi \frac{\mathbf{a}_2 \times \mathbf{a}_3}{\mathbf{a}_1 \cdot (\mathbf{a}_2 \times \mathbf{a}_3)}, \quad \mathbf{b}_2 = 2\pi \frac{\mathbf{a}_3 \times \mathbf{a}_1}{\mathbf{a}_1 \cdot (\mathbf{a}_2 \times \mathbf{a}_3)}, \quad \mathbf{b}_3 = 2\pi \frac{\mathbf{a}_1 \times \mathbf{a}_2}{\mathbf{a}_1 \cdot (\mathbf{a}_2 \times \mathbf{a}_3)} \tag{2.17}$$

These vectors are the Fourier transform of the primitive lattice vectors and define the reciprocal space or **k**-space. Using these vectors every reciprocal lattice site can be given by the reciprocal vector **G**:

$$\mathbf{G} = h\mathbf{b}_1 + k\mathbf{b}_2 + l\mathbf{b}_3 \tag{2.18}$$

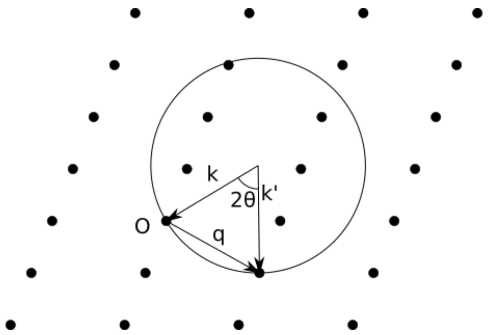

Figure 2.5: Incident wave vector k hitting particle at position O, diffracted wave vector k', scattering vector q and the angle between incident and scattered wave 2θ. Modified figure originally taken from [46].

Where h, k and l are integers. The product of a basis-vector and reciprocal basis vector is:

$$\mathbf{b}_i \cdot \mathbf{a}_j = 2\pi\delta_{ij} \tag{2.19}$$

where $\delta_{ij} = 1$ if $i = j$ and $\delta_{ij} = 0$ if $i \neq j$. These are also known as the Laue equations and must be met for $b_1 \cdot a_1, b_2 \cdot a_2$ and $b_3 \cdot a_3$ for there to be diffraction [29]. So the vector product between the reciprocal and translation vector becomes:

$$\mathbf{G} \cdot \mathbf{R} = 2\pi(hn_1 + kn_2 + ln_3) \tag{2.20}$$

where the sum $(hn_1 + kn_2 + ln_3)$ is an integer and the phase term of the scattered ray, $e^{i(\mathbf{G}\cdot\mathbf{R})}$, equals 1. When the scattering vector **q**, from (2.12), is equal to a reciprocal vector **G** the condition for constructive interference are met. This happens when the scattering vector **q** goes from one reciprocal lattice point to another. A way of illustrating this is using the Ewald sphere. Here a sphere is drawn around a point in reciprocal space with the radius of $k = 2\pi/\lambda$. The diffracted wave also has the length $2\pi/\lambda$ so for the scattering vector **q** to be equal to **G** two or more lattice points must be on the Ewald sphere. A two dimentional version of this can be seen in figure 2.5. In a solid crystal these conditions are hard to meet and therefore it is necessary to do a systematic sweep to get noticeable diffraction.

Under elastic scattering the energy $\hbar\omega$ is conserved. Therefore the frequency of the scattered ray, $\omega' = ck'$, is the same as the incident and the magnitude of the wavevectors k and k' are equal. From this, $G = Q$ and 2.12 the diffraction condition can be written as $(\mathbf{k} + \mathbf{G})^2 = \mathbf{k}'^2$ or:

$$2\mathbf{k} \cdot \mathbf{G} + G^2 = 0 \tag{2.21}$$

Since $-\mathbf{G}$ is also a reciprocal vector, the equation 2.21 can be written as:

$$2\mathbf{k} \cdot \mathbf{G} = G^2 \tag{2.22}$$

from this it is possible to find the distance $d(hkl)$ between parallel lattice planes, or phyllosilicate sheets in the case of smectite, normal to the direction $\mathbf{G} = h\mathbf{b}_1 + k\mathbf{b}_2 + l\mathbf{b}_3$

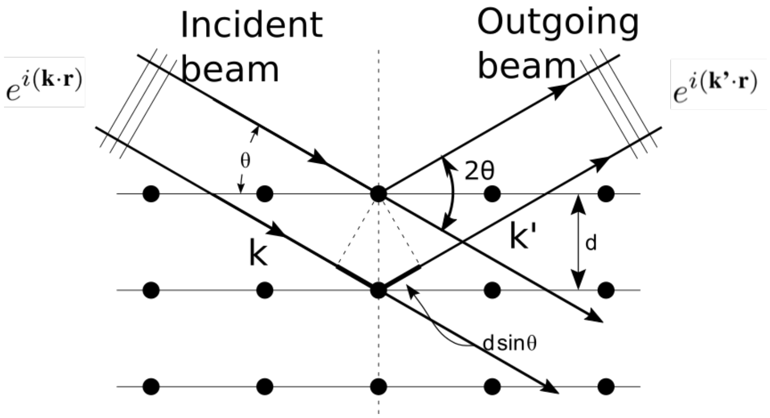

Figure 2.6: Figure illustrating scattering from a crystal volume dV. Here the incident beam is scattered and emerges with a new wavevector k'. One can also see the scattering angle as 2θ compared to the incident angle. There is also a relation between distance d between crystal-planes and the angle for constructive interference. More on this at the end of current section. Modified figure originally from [26]

[29]:

$$d(hkl) = 2\pi/|\mathbf{G}| \tag{2.23}$$

Putting this into equation (2.22) gives:

$$2(2\pi/\lambda)\sin\theta = 2\pi/d(hkl) \tag{2.24}$$

Which can be rewritten as Bragg's law:

$$2d\sin\theta = n\lambda \tag{2.25}$$

Which is the condition for coherent scattering from a crystal lattice. An illustration of this can also be seen in figure 2.6. As the scattering vector **q** is equal to the reciprocal vector **G**, using equation (2.23) the magnitude of **q** can be given by

$$q = 2k\sin\theta = \frac{4\pi}{\lambda}\sin\theta \tag{2.26}$$

It becomes natural to describe the scattering in terms of the magnitude of **q**, as opposed to 2θ, since it is independent of wavelength, which can vary between instruments.

2.2.5 Powder diffraction

Using the diffraction it becomes possible to measure distances between the layers in clay. Using Bragg's law (2.25), and (2.26). With a known wavelength and the angle with the highest measured intensity, Bragg peak, and equation 2.26, the layer spacing $d(001)$ form the diffraction pattern is:

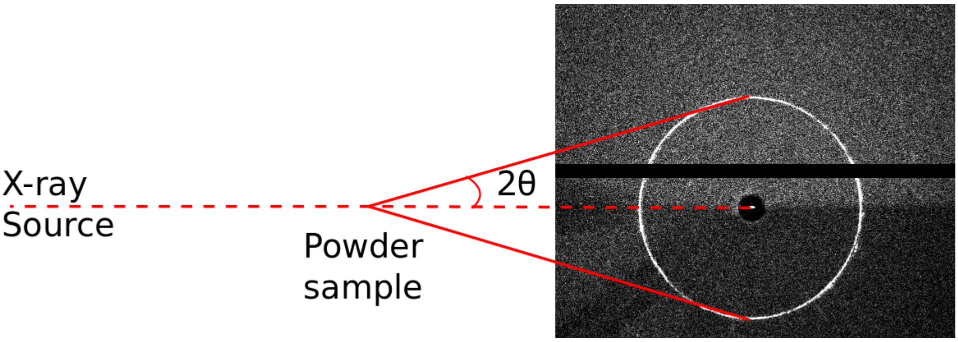

Figure 2.7: Here the X-rays from the source goes through the powder sample and creates a Debye-Scherrer cone and a diffraction ring is measured at the detector. Diffraction ring from a "wet" NiFh sample, Fluorhectorite (2.1) with M=Ni and $x = 0.5$

$$d(001) = \frac{2\pi}{q_c} \tag{2.27}$$

This is the technique used in XRD to measure the structure of crystals and structures with repeating pattern on a molecular scale. Here the sample is in powder form. This makes it much simpler to meet the Laue conditions for diffraction. In a single crystal it has to be in the correct position for diffraction, for a powder however there is nearly always a crystal or, in this case, a stack of silicate sheets in the correct position. Then incident waves, which are perpendicular to the plane of the detector, are scattered in an evenly spread in a cone around the incident beam. This cone is called the Debye-Scherrer cone [1] and the angle between incident **k** and scattered **k'** wavevector is 2θ as seen in figure 2.7.
In addition to the diffraction conditions there are some other factors involved in the measured intensity.

2.2.6 Intensity

The measured intensity $I(\mathbf{q})$ is dependent on peak position q, structure factor $S(q)$, Lorentz-polarization factor $L_p(\mathbf{q})$ and interference function $\Phi(\mathbf{q})$[12, 33]:

$$I(\mathbf{q}) \propto |S(\mathbf{q})|^2 L_p(\mathbf{q}) \Phi(\mathbf{q}) \tag{2.28}$$

Structure factor of Fluorohectorite

For a clay material the structure factor is given by[1]

$$S(\mathbf{q}) = \sum_{j=1}^{n} n_j f_j e^{i\mathbf{q}\cdot\mathbf{r}_j} e^{-W_j\left(\frac{\mathbf{q}}{4\pi}\right)^2} \tag{2.29}$$

Where f_j is the atomic scattering factor, n_j is the number of j type atoms located at $\mathbf{r}_j$ from the center of symmetry along (00l) axis. The summation of the atomic form factors e is taken over the unit cell. The exponential term is the Debye-Waller temperature correction factor. The Debye-Waller factor is the reduction in scattered intensity due to lattice vibration, which is dependent on temperature. The term is found from the temporal average of atoms position. Taking into account the centrosymmetric structure of Fluorhectorite, there is a atom at both **-r** and **r** from the center of the structure, and the identity: $e^{i(\cdot \mathbf{r}\cdot\mathbf{q})} + e^{-i(\mathbf{r}\cdot\mathbf{q})} = 2\cos(\mathbf{q}\cdot\mathbf{r})$, the structure factor (2.29) can be rewritten as

$$S(\mathbf{q}) = 2\sum_{j=1}^{n} n_j f_j \cos(\mathbf{q}\cdot\mathbf{r}_j) e^{-W_j\left(\frac{\mathbf{q}}{4\pi}\right)^2} \tag{2.30}$$

Polarization Factor

The Lorentz-polarization factor $L_p(q)$ is given by

$$L_p(\mathbf{q}) = \frac{P}{\left(\frac{\lambda q}{4\pi}\right)^{\nu+1}\sqrt{1-\left(\frac{\lambda q}{4\pi}\right)^2}} \tag{2.31}$$

Where P is the polarization contribution due to the X-ray source. The value of ν is in general given by the amount of crystals oriented so that the diffracted rays are directed into the detector. ν takes a value between 1, for perfect powder, and 0, for a perfect crystal [1]. Here it is used when referring to clay powder and its orientation which should ideally be 1.

Pseudo-Voigt

The intensities of the Bragg peaks are plotted as a function of q. To obtain an accurate Bragg peak position a pseudo-Voigt peak shape function is used on the data. This function provides an approximation to the convolution of Lorentzian and Gaussian functions [12]

$$\Phi(q) = \eta\frac{2}{\pi}\frac{\gamma}{4(q-q_c)^2+\Gamma^2} + (1-\eta)\frac{\sqrt{4ln2}}{\sqrt{\pi}\Gamma}exp\left[\frac{-4ln2(q-q_c)^2}{\Gamma^2}\right] \tag{2.32}$$

The interference function, $\Phi(q)$, is associated with the measured intensity. Γ is the width of the half maximum of the experimental peak and η is a mixing constant, between 0 and 1, changing the shape of the experimental curve from a Gaussian to Lorentzian function. η is given by

$$\eta = 1.36603\left(\frac{\omega_L}{\Gamma}\right) - 0.47719\left(\frac{\omega_L}{\Gamma}\right)^2 + 0.11116\left(\frac{\omega_L}{\Gamma}\right)^3 \tag{2.33}$$

$$\Gamma = \left(\omega_G^5 + 2.69269\omega_G^4\omega_L + 2.42843\omega_G^3\omega_L^2 + 4.47163\omega_G^2\omega_L^3 + 0.07842\omega_G\omega_L^4 + \omega_L^5\right)^{1/5} \tag{2.34}$$

2.3 PID-controller

A proportional–integral–derivative controller(PID-controller) is the control loop feedback system mechanism used to control the temperature of the sample. The general equation for a PID-controller is given by

$$u(t) = K_p(x(t) - y(t)) + K_i(\int_0^t x(t')dt' - \int_0^t y(t')dt') + K_d(\frac{dx(t)}{dt} - \frac{dy(t)}{dt}) \quad (2.35)$$

Where $u(t)$ is the controller output, $x(t)$ is the control input, $y(t)$ is the output while K_p, K_i and K_d are proportional constants. Introducing the variable $e(t) = x(t) - y(t)$, the equation can be rewritten as

$$u(t) = K_p e(t) + K_i \int_0^t e(t')dt' + K_d \frac{de(t)}{dt} \quad (2.36)$$

The system works through the calculation of an error value, $e(t)$, and the following correction to the control output($u(t)$) in order to minimize said error [11]. This correction is in proportion to the proportional(P), integral(I) and derivative(D) terms of $e(t)$. The error value here concerns the difference between the desired temperature and measured temperature $(e(t) = x(t) - y(t))$. A block diagram of this type of control loop can be found in figure 2.8.

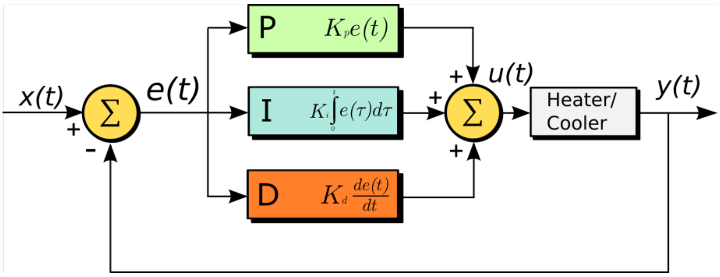

Figure 2.8: Here a typical block diagram for a PID-controller can be seen. Modified figure originally found at [45]

To find the optimal values for K_p, K_i and K_d the Ziegler–Nichols Method can be used. Where the proportional gain K_p is increased until the the ultimate gain K_u is found. At which the output has stable and oscillates with period T_u with constant amplitude. Then the tuning rules are given by table 2.1[11].

	K_p	K_i	K_d
P	$0.5K_u$		
PI	$0.45K_u$	$1.2/T_u$	
PID	$0.6K_u$	$2/T_u$	$T_u/8$

Table 2.1: Tuning rules for the Ziegler–Nichols Method

Chapter 3

Methods

This chapter contains the specific description the different parts of the experimental setup and the Labview code used to control temperature and log the time, temperature and pressure. Along with the description of the three experiments that were done using the setup.

3.1 X-ray home station

The X-ray diffraction measurements were performed on a Bruker NanoSTAR X-ray scattering instrument. With the X-ray source being a attached to a Xenocs GeniX stationary electron impact source. The electrons are accelerated over a voltage of 50 kV and have a current of 1 mA. The X-rays are collimated and are made monochrome through an elliptical mirror with a multi-layer coating. The rays are reflected and due to the focus at infinity made parallel. The multilayer-coating only reflects wavelengths satisfying Bragg's law (2.25). This creates a natural band-pass and which in this case only lets through Cu-K_α rays, with a wavelength of 1.5406 Å. The incident angle changes along the mirror and therefore the multi-layer is graded so that it still satisfies Bragg's law at all points [47].
After the reflection the now close to monochrome rays pass through, if the shutters are open, a Bruker NanoSTAR collimation system. The system then creates a circular spot with a diameter of 400 μm. The rays enter the X-ray chamber, where the sample is placed, and exits the chamber into the detector. The chamber is approximately 27 cm×22 cm×29 cm(depth×width×height) with a platform on a mechanical arm capable of moving in x and y direction perpendicular on the X-ray(z) direction with the smallest step being 0.1 mm. The chamber has a large door made of radiation proof glass and three holes on the back side. One for electrical wires controlling the arm and two others here used for a draining tube, gas tube and electrical wires and the largest used for the circulator tubes which can be seen in figure 3.3.

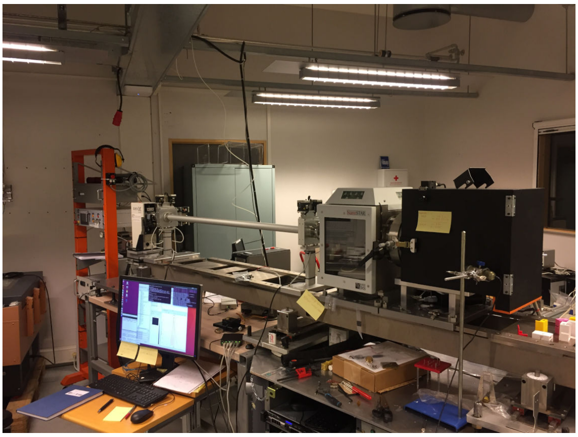

Figure 3.1: The inhouse X-ray machine.

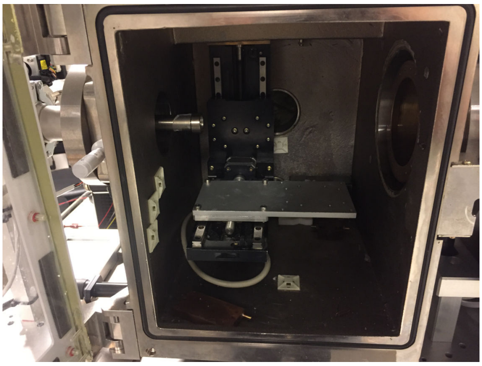

Figure 3.2: Opened X-ray chamber. Here the box is empty except for the mechanical arm.

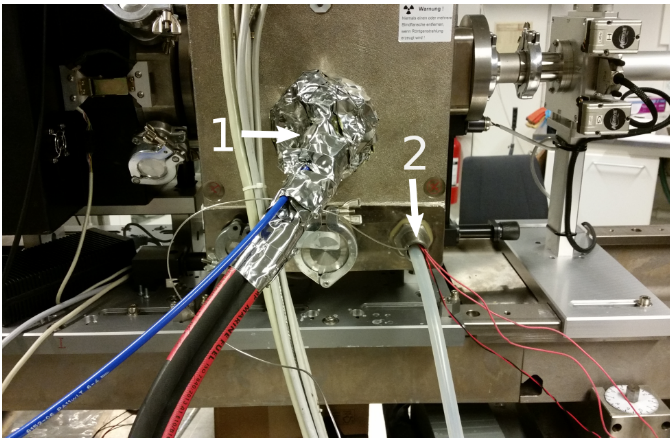

Figure 3.3: Back of the sample chamber. Here with the two sets of wires/tubes used for this experiment are marked. 1: The tubes for the circulation cooler and the smaller nitrogen tube. Both thoroughly covered in lead tape at the entry. 2: The draining tube, the electrical wires for heating element, the Peltier-elements and the metal gas tube.

3.2 Detector

The detector being used was of the type DECTRIS PILATUS3 R 200K-A Detector system. This detector has a 450 μm thick silicon sensor which operates in single photon counting mode. Where X-rays are converted to electric current, as illustrated i figure 3.4, on a two dimensional array of pn-diodes. The detector works through the photoelectric effect where an incident photon excites one or more electrons. These electrons then drifts over through the electric field in the diode and creates a current proportional to the intensity with a maximal count rate of 10^7 photons per second. Each pixel, pn-diode, is $172 \times 172\mu\text{m}^2$ and placed on an array with 487×407 pixels. This gives a 198 209 pixels covering 83.8×70.0 mm^2. The quantum efficiency of the 450μm detector for Cu radiation of 8 keV is at 98%, meaning it counts 98% of the radiation at this energy [14]. The detector also has an energy range of 3.6 to 36.0 keV and a frame-rate of 20 Hz. The detector is made out of two modules on top of each other with a tiny space between them. This tiny space manifests as a black stripe on the diffraction images, as seen in figure 2.7. The pixels in this space is set to a value of -1 and can be seen clearly in figure 3.23.

WAXS

The distance between sample and detector can be changed switching from small-angle X-ray scattering (SAXS) to wide-angle X-ray scattering (WAXS) measurements. In this experiment the detector is placed in the wide-angle position. The angles the detector is able to observe are 0.6322° from the beam-stop to the edge of the detector at 8.089°.

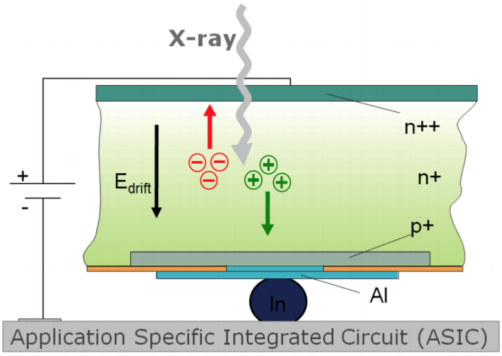

Figure 3.4: Here the incident X-ray photon is absorbed by the electrons in silicone diode and transported over the electric field and creating a current. Image courtesy of Decteris [13].

3.3 Sample cell and calibration

3.3.1 Sample cell

A glass capillary is filled with a clay sample and then glued into a ferrule and mounted on a cell which again is mounted on a goniometer. The goniometer is then placed on a 90 ° angle attached with screws in a groove on the heating/cooling rig. The capillary is brought above a copper plate with an extruding section place upon a stack of Peltier-elements on top of a copper platform.

The capillaries are made of glass and are 5 mm in diameter with a wall thickness of 0.01 mm. They are originally 80 mm long but have been shortened to about 30 mm using a gas burner. After the clay is filled in the capillari a small amount of glass wool is pushed in after it. This is to prevent the clay from being sucked out when the vacuum pump is turned on. For the X-ray diffraction a copy of the sample cell used in [10] was created. Only there they used sapphire capilaries. However since they are quite expensive and the capilaries needed to be shortened we setteled for glass capilaries. The cell consist of a Swagelok Tee union with one opening connected to the gas system. Another opening is closed and to the last the glass capillary is fastened in a ferrule with the two component epoxy adhesive Loctite EA 3450. On the other side a tap is welded on and used to fasten the cell to a goniometer. A picture of the sample cell can be seen in figure 3.6.

3.4 Heating and cooling system

The glass capillary is heated and cooled when brought into contact with a copper plate. The heating is done with two 20 W heating element fastened to the copper plate. The copper plate is 30 mm × 45 mm with an 20 mm elevated section in the middle perpendicular to the X-rays and parallel to the glass capillary.

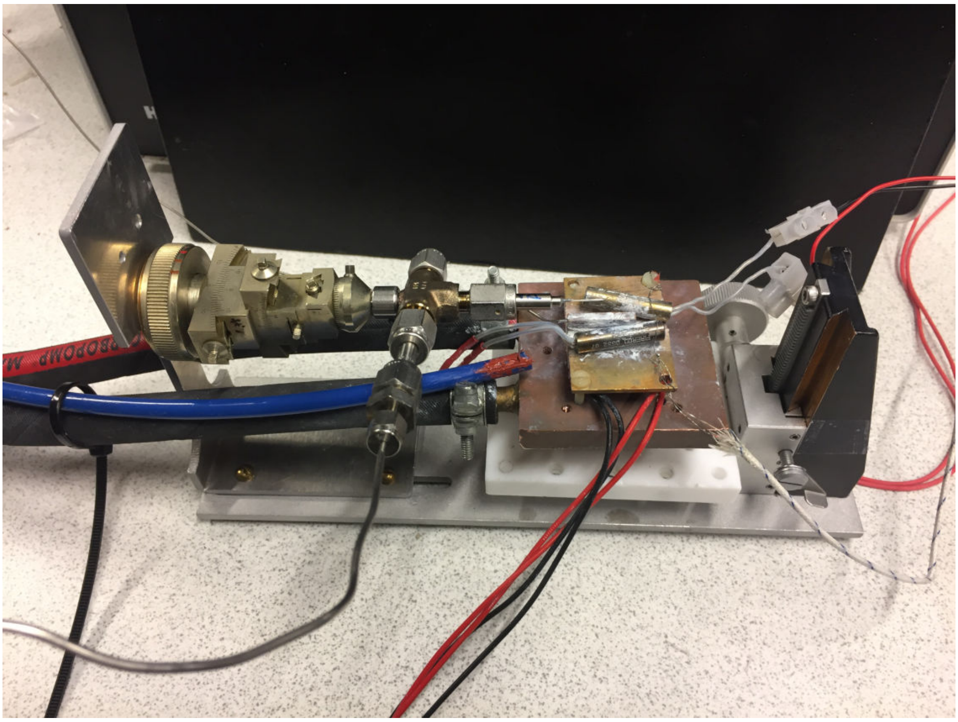

Figure 3.5: The sample cell mounted on the experimental setup. Outside of the X-ray chamber. The platform at the base is 25 cm long.

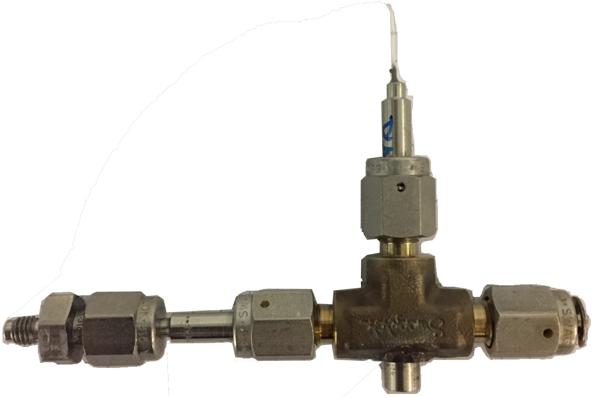

Figure 3.6: Sample cell with glass capillary filled with clay. Here a Swagelok Tee union is closed on one side, connected to the gass system through a 1/16 inch tube and a shortened 0.5 mm glass capillary fastened on the entrance pointing upward. At the bottom a tap is welded on in order to fasten it to a goniometerhead.

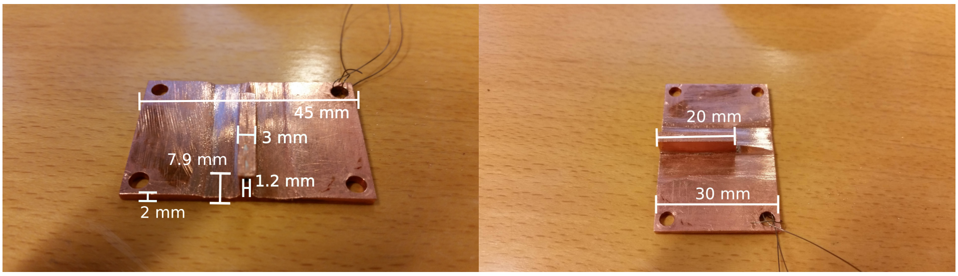

(a) **(b)**

Figure 3.7: The copper plate on placed on top of the Peltier stack. With filed down sections at each side of the extruding part for placing the heating elements.

This plate is placed atop of two peltier elements, in a stack connected in series, and screwed onto a larger copper platform with nylon screws. The larger copper platform has internal pluming for the coolant and is connected to the circulator cooling system through he two tubes that goes in the back of the X-ray chamber. The Peltier elements and circulation cooler are used together to achieve a sub room temperature on the sample. The circulation cooler can lower the temperature of the large copper plate to 263 K. Any lower than that the Peltier elements are used in combination with the circulator. The circulator is of the type Haake G with a modified Haake D8 immersion circulator. The circulator target temperature is voltage controlled through a mini-jack input with range of -10V to 10V corresponding to 173 K to 373 K. The cooling liquid was a mix of approximately 50:50 water and ethylene glycol based antifreeze. This combination have a freezing point at 237 K. A Peltiere element is an electrical component using the Peltier effect to convert electricity into heat. This effect is the cooling of one junction and the heating of another when running current through a circuit of two dissimilar conductors [15]. This effect is relative to the temperature on the warm or cold side. Here two Peltier elements are placed in a stack and are connected in series to create an even bigger temperature gradient between the warm and the cold side. This results in the top of the stack has a significant lower temperature compared with the cooled copper plate on the warm side of the Peltier stack. The peltier element used here is a GM250-71-14-16 Seebeck Effect Module. With effect of 2.9 W, max current of 1.1 A, max voltage 5.3 V and a surface area of 30 mm×30 mm. The Seebeck effect is the reverse effect of the Peltier effect. Where heat difference creates a current [16].

The large copper plate is mounted on a piece of insulating plastic which can be raised to be in contact with the glass capillary containing the clay sample. During the experiment a box is placed around the peltier and copper stack. The box is there to contain a nitrogen stream which is set up to prevent air moister form freezing on the capillary and obscure the measurements. The box also serves to protect the detector in case of the glass capillary bursting. This box has a window on each side so that the X-rays can travel through. Both windows are covered with kapton tape. There is also two other openings, one for the electrical wires to the Peltier elements and one for the heating element, thermocouple

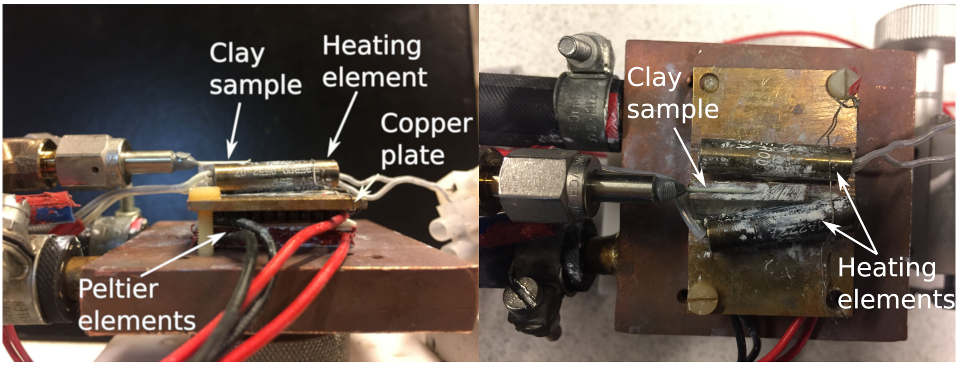

(a) **(b)**

Figure 3.8: The sample cell placed in contact with the copper plate on top of a stack of Peltier-elements on a movable platform. Seen from the incident X-ray direction,3.8a, and from above, 3.8b. With added markers for the capillary with the clay sample, copper plate, heating elements, and Peltier-elements.

and glass capillary. The nitrogen stream goes through a hole in the side made with a drill. The box is made with a 3D-printer and is made out of PolyLactic Acid(PLA). PLA has a melting point of about 453 K to 493 K. This is well above the target temperature of 423 K required to dry the clay properly. It does however start to deform at high temperature so the drying is done before the box is placed above the sample.

3.5 Gas, Pressure and Vacuum

Carbon dioxide gas is provided through a 50 L, 50 bar gas cylinder. CO_2 provided by AGA with 100% purity. This container is connected to the sample through a series of tubes with Swagelok connections. The pressure on the sample is supplied by a Teledyne ISCO D-series syringe pump connected to the carbon dioxide cylinder. To evacuate the system of air and water vapour, under activation(drying) of the clay sample, the system is also connected to an Edwards RV12 Vacuum Pump through a union tee fitting. A diagram of the connections are shown in figure 3.11. Reducer fittings are not shown in the diagram. The reducers converted from a 1/8 inch tube to a 1/16 inch for the carbon dioxides path form cylinder to sample. The pressure rating of the system is 172 bar, where the weak points are the SS-41GS2 valves not counting the glass capillary at the end of the system. Here the pressure rating would be dependent on how well the capillary was shortened and the glue fastening the sample to the rest of the gas system. The capillary holds at least up to 50 bars and under a pressure test held up to 80 bars before bursting. For the vacuum a conversion from a 25 mm steel tube to a 1/16 inch tube via an 1/4 and an 1/8 inch Swagelok reducer fitting was used. The vacuum is measured on a Vacuubrand VAP 5 with a range from 1000 mbar to 10^{-3} mbar. In addition to CO_2 a tank of Nitrogen was used, also 100% purity and 50 bar, provided by AGA.

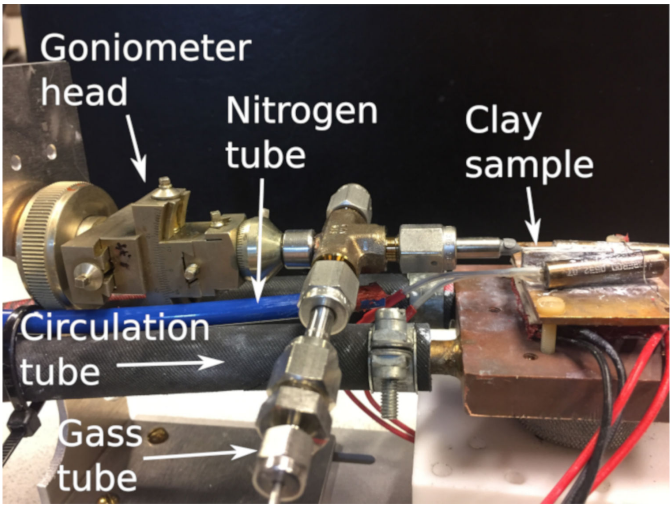

Figure 3.9: Sample cell, connected to the gas tube, mounted on the goniometer head as indicated in figure. The circulation tubes connected to the copper platform.

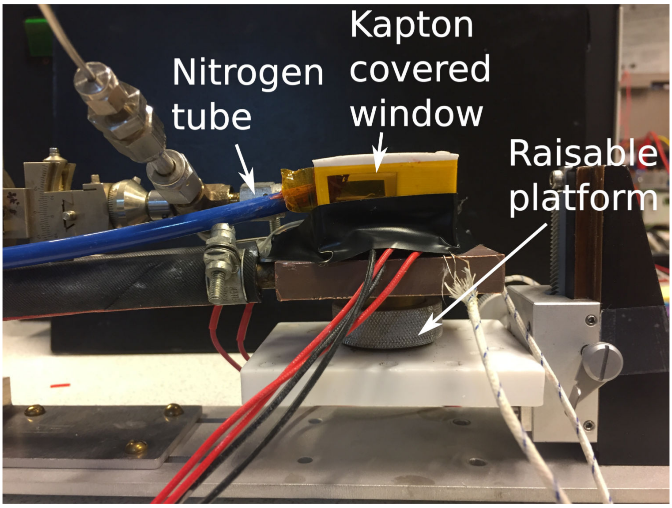

Figure 3.10: Plastic box around the clay sample with kapton covered windows on both side and a tube supplying nitrogen during experiments under 273 K.

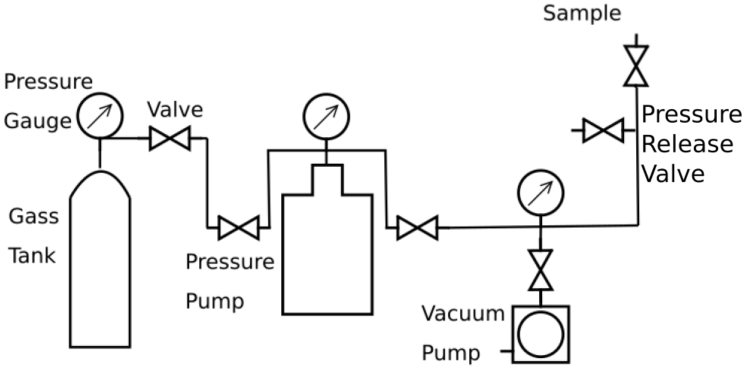

Figure 3.11: Diagram of the connected gas tank, pressure pump and vacuum pump with associated valves and pressure gauges.

The pressure is measured through a Keller PA-23s. The Keller sensor is a piezoresistive pressure transmitter, has a range of 0 to 400 bar, with an supposed output range of 0 to 10 V, a direct current voltage supply between 13 to 28 and maximum current of 5 mA. The lowest this Keller sensor was able to measure was 1.73 bars. Under that the vacuum sensor is used to confirm 0 bars/vacuum. Both pressure and vacuum pumps and valves for CO_2 and N_2 were handled manually during the experiments.

3.6 Power supply

Here two different power supplies are used. The first, is of type Delta Electronika ES150, with maximal voltage output of 15 V and maximal current output of 10 A. The second of type, is used to drive the pressure gauge with the possible output of 15 V, -15 V or 5 V at a current of 250 mA, 250 mA and 1000 mA respectively. The power supplies can be seen in figure 3.13a and 3.13b. The current from the first power supply, Delta Electronika, is voltage controlled with a voltage between 0 and 5 V corresponding to a current between 0 and 10 A.

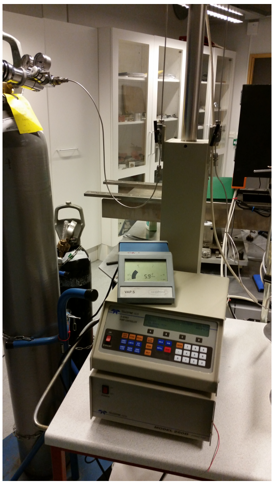

Figure 3.12: Teledyne pressure pump connected to the CO_2 cylinder and the Vacuubrand vacuum gauge resting on top of it.

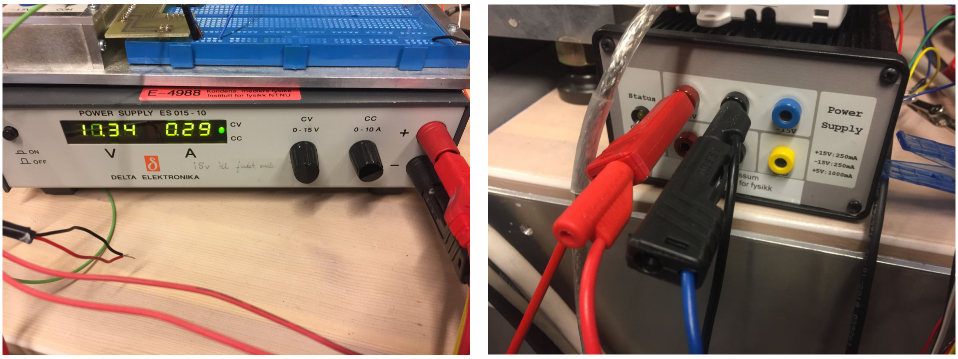

(a) First power supply

(b) Second power supply

Figure 3.13: The two power supplies used. Power supply (**a**) is used to drive heater and Peltier-element and is controlled through a DAQ device. Here pictured with a breadboard on top of it and connected to a DAQ device. Power supply (**b**), used to drive the pressure gauge.

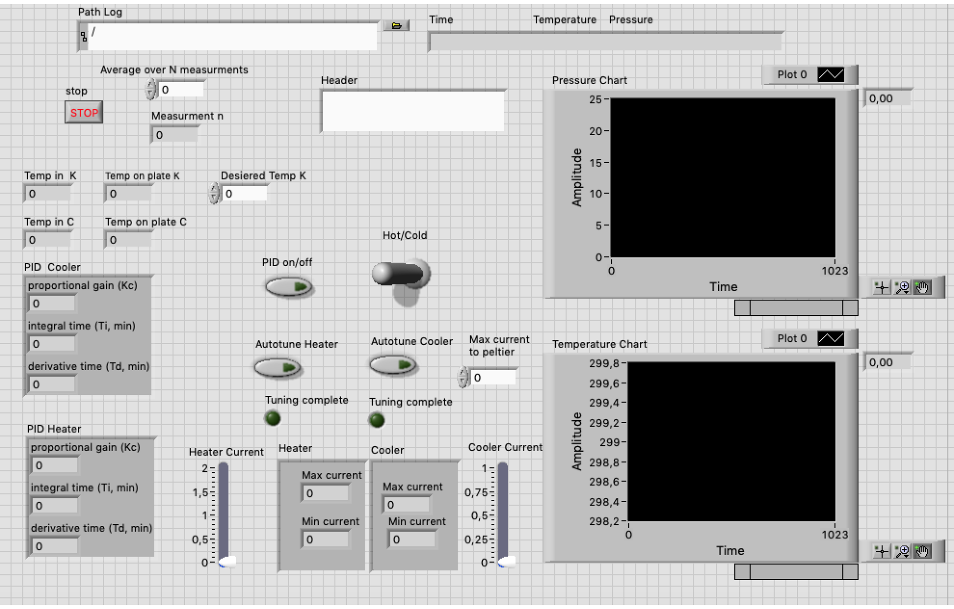

Figure 3.14: Labview front panel of the temperature control.

3.7 Data Acquisition and Labview

Control of the sample temperature, measuring of said temperature and the sample pressure was done with a National Instrument USB-6211 multifunctional I/O data acquisition(DAQ) device. Two DAQ devices of the same model was used in the experiment. One to control the first power supply and target temperature on the circulation cooler, as seen in figure 3.13a and second for measuring temperature and pressure on the clay sample.

To communicate with the DAQ's through a computer the program LabVIEW was used. Laboratory Virtual Instrument Engineering Workbench(LabVIEW) is a visual programming cross platform software developed and released by National Instruments[37]. First released in 1986 with subsequent near annually new releases or updates. Here the 2017 version(Labview 17) was used. The program creates a text-file of temperature and pressure measurements along with a time-stamp for the measurement. The temperature and pressure was averaged over a selected number, N, of measurements, here $N = 100$ was used. Labview was running on a different computer than the XRD measurements so their clocks needed to be synchronized. Code for matching time-stamps and XRD-images is included in appendix A. In addition to logging of measurements the program controls the heating elements and cooler system and displays the averaged measurements to the front panel. The front panel can be seen in figure 3.14. The program consists of two while loops. One within the other and a sequence of measurements in the innermost loop. A total overview of the Labviews Virtual Instrument(vi) file can be seen in figure 3.15, with boxed into different section according to function.

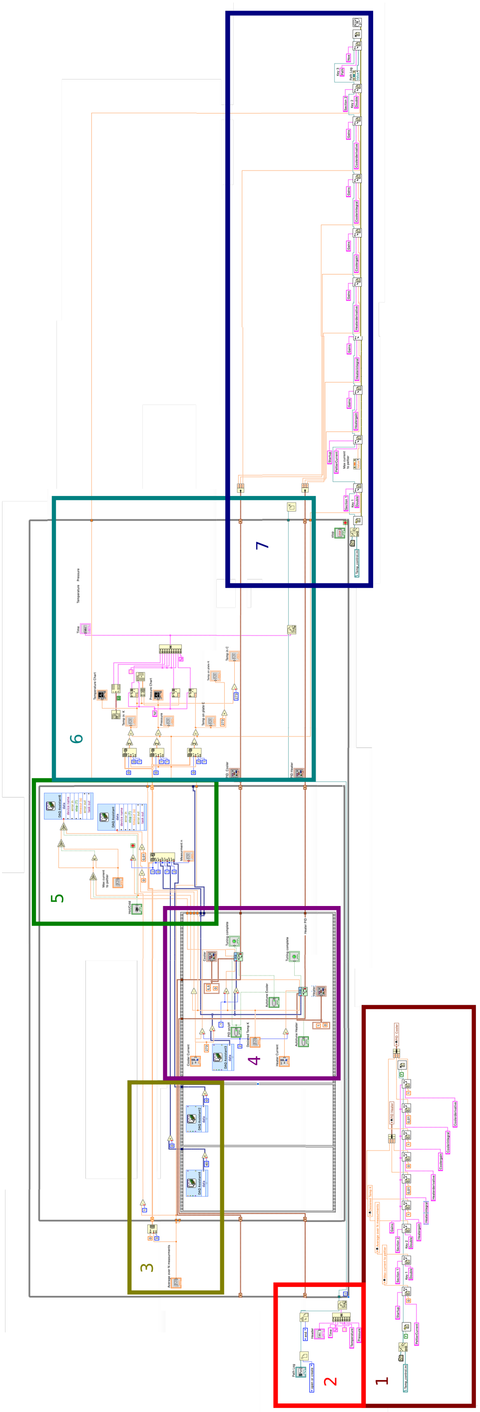

Figure 3.15: Labview Block Diagram with the major parts in 7 numbered squares, each square is responsible for a different part of the program.

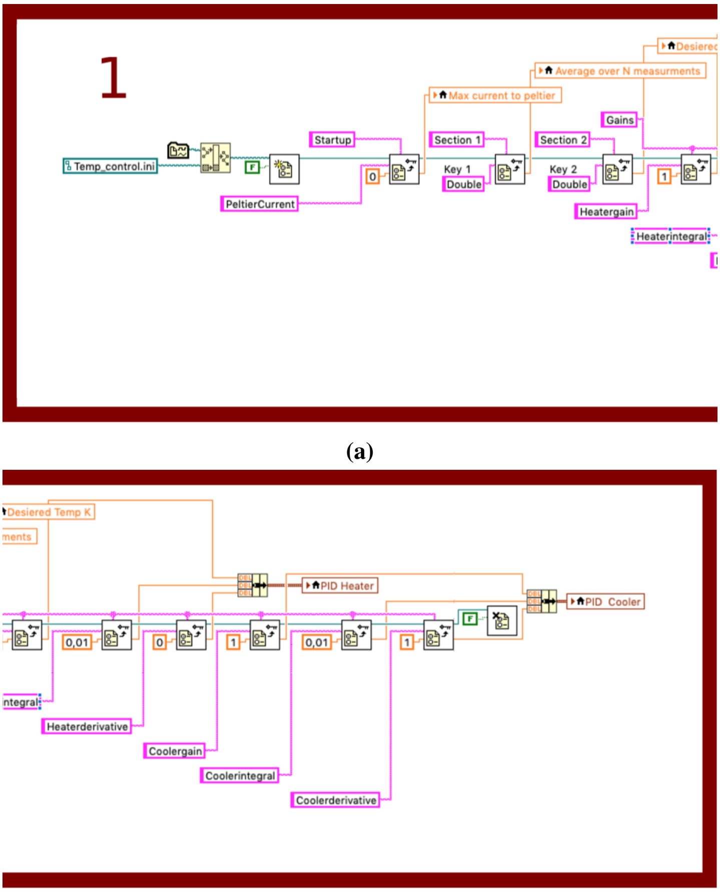

(a)

(b)

Figure 3.16: Labview code. First part of the code where the configurations for the program are loaded from an existing ".ini" file or loading deafult values.

Square 1. Load configuration

When the program starts it loads the values for the Heater and Cooler PIDs, the number of measurements the program takes the average over, the desired temperature of the copper plate and the maximum current to the Peltier-elements. Labview code for this can be seen in figure 3.16.

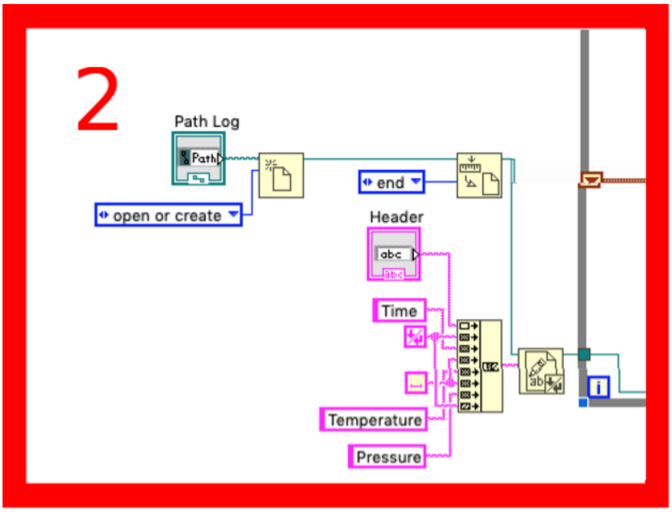

Figure 3.17: Open or creating a text file to save the measurements, with a header and an additional optional header for comments.

Square 2. Create/open file.

For each time the Labview program runs the measurements were logged into a text(.txt) file. This file is either created by the program or opened in the case of an existing file. In the case of an existing file the measurements are appended. There is also an additional header to add comments to the subsequent measurements. The path of the file then goes into the first while loop. The Labview code for this can be seen in figure 3.17.

Square 3. Start averaging loop

Inside the first while loop a second while loop is created. This loop runs N times where and the measurements made inside it is stored in a $3 \times N$ matrix. Inside the second while loop there is a flat sequence structure. In the first frame the pressure on the clay sample is logged. The sensor has a output range of 0-10 V and is able to measure 0 - 400 bars of pressure. The output of the sensor is therefore scaled with 40 before the measurement is stored. The second frame is the temperature measured by a thermocouple resting on the copper plate. Both measurements are done with a DAQ unit.

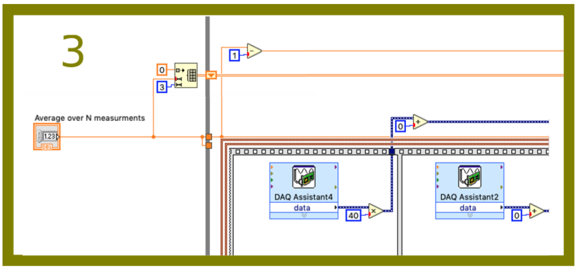

Figure 3.18: Inside the first labview while loop a matrix is created for storing measurements. Inside a sequence structure the pressure is measured, then the temperature on the copper plate is measured.

Square 4. Measuring temperature and PID-controller

In order to keep the samples at the desired temperature a combination of heating and cooling systems is used. Two heating elements are placed on the copper plate, which the mounted clay sample is in thermal contact with. Stable temperature is achieved using Labviews PID-control with a controlling input. Namely desired temperature and maximal and minimal output current. In addition to this the PID controllers have two Boolean inputs. One "PID on/off" is for turning from manual temperature control to automatic control and a second for auto-tuning off the system. When the auto-tuning is turned on the system will find the proportional gains and integration, T$_i$, and derivation time, T$_d$, through the Ziegler-Nichols method. The PID controllers also returns the settings for the PID after auto-tuning.

The Peltier elements and circulation cooler are used together to achieve the desired temperature. The cooler gets a direct input, through Labview, to go to the desired temperature. This is often impossible for the cooler to do on its own, then the Peltier-elements make up for the difference. The Peltier stack is controlled as the heating element, using the Labview Temperature PID. This time with the negative input of both measured and desired temperature. This is because the PID is created for heating up to the desired temperature and then turning of when the temperature is to high. With a negative input the PID believes it heats from e.g -293 K to -273 K and turns off when the temperature gets "too high". There is also the option of manually controlling the current to the Peltier-elements and heating elements.

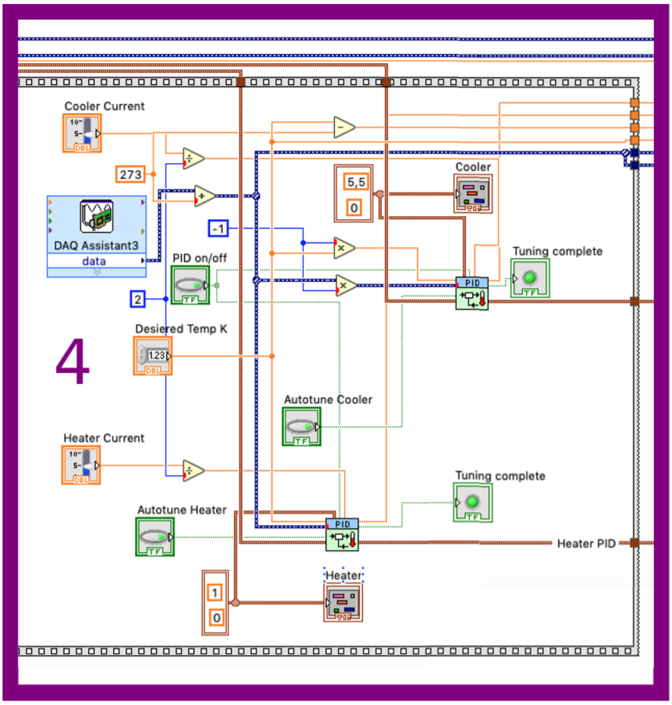

Figure 3.19: Here the input from the thermocouple, through the "DAQ Assistant3", goes into the sequence step. The measured temperature and the desired temperature goes into both PID controllers and the output is passed through the sequence step. In addition to the temperature both PIDs have a max and min value for the output. There are also an option to auto-tune the PIDs and assume manual control of the Peltier-elements and heating elements.

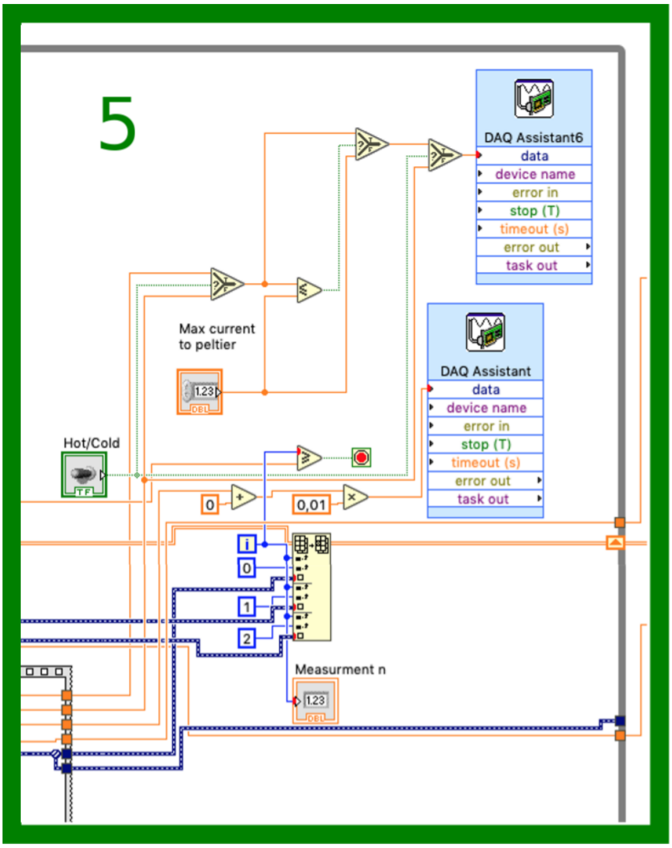

Figure 3.20: Output from square 4(figure 3.19) and square 3(figure 3.18) comes out through the sequence structure and is stored in the measurement array. The array is then passed to the next iteration of the while loop through a shift register. The "DAQ assistant" controls the circulator. Depending on whether the program is set to Heater or Cooler mode the "DAQ assistant6" gives current to the heating elements or the Peltier-elements.

Square 5.

The output from the PID-controllers in square 4, figure 3.20, is given to the DAQ. Depending on whether it is in Heating or Cooling mode the "DAQ Assistant6" gets the signal for the heating element or the Peltier-elements. The output is voltage, used to control the power supply connected to the either the heating element or the Peltier-element. There is also a safety condition so that the maximum output from the power supply is 1.10 A. The second DAQ, "DAQ Assistant", receive the desired temperature in Celsius scaled by 0.01 and controls the circulation cooler. The measurements from the sequence structure are stored in the measurement array.

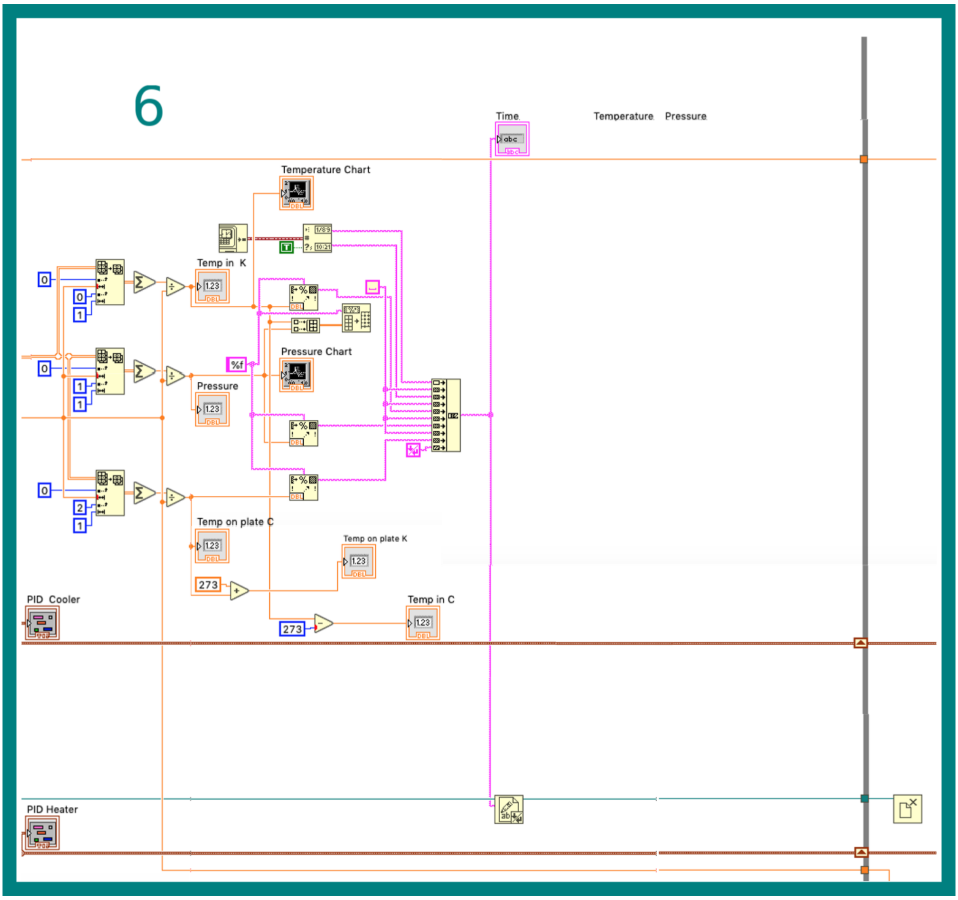

Figure 3.21: The average of the measurements from innermost while loop are written to file and the Front panel along with a time stamp. The settings for the PID controls are passed to the next iteration through a shift register.

Square 6.

The array containing the measurements are passed through the innermost while loop. The average of the pressure, temperature both inside the copper plate and on top of the plate is stored, alongside the time stamp, in a text-file. The average is found through the sum of the array subset containing the respective measurement and dividing it by the length of the subset. They are also written to the screen through a graph and indicators for temperature and pressure. The measurement array is then passed to the next iteration of the loop through a shift register. The same goes for the settings for the PID controls which are also passed to the front panel where they can be viewed.

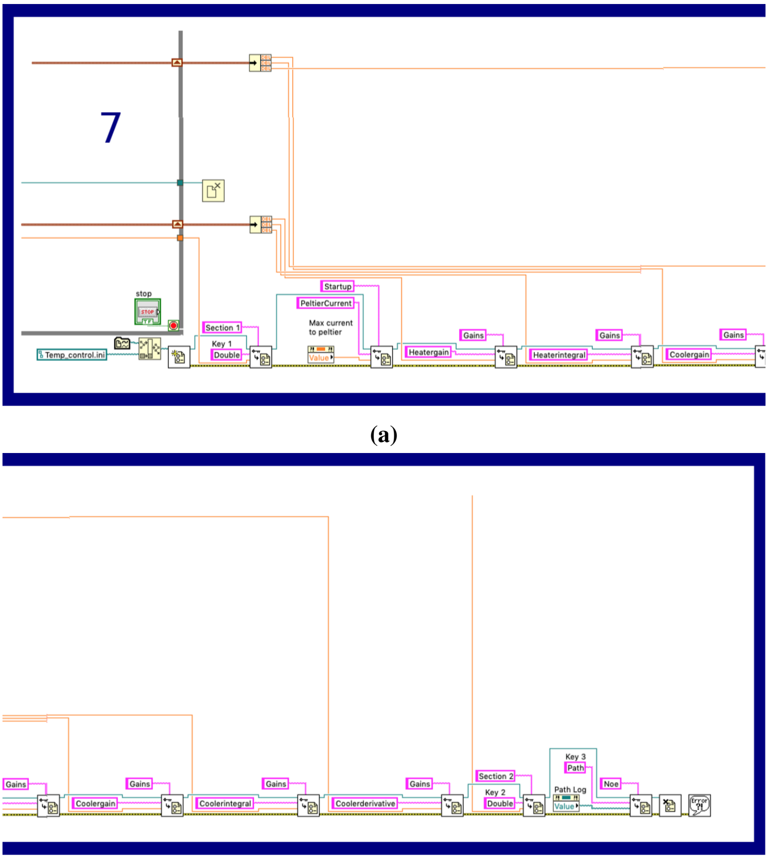

(a)

(b)

Figure 3.22: Labview code where the configurations of the VI is stored in a Temp_control.ini file. The specific values stored here are the parameters for the heater and cooler PIDs, the maximum current to the Peltier elements and desired temperature on the copper plate.

Square 7.

The last part of the program, as seen in figure 3.22, the text-file with the measurements are closed and the PID settings are stored in a configuration file along with the desired temperature and maximum Peltier current. This is done so that the program can be momentarily stopped and started again and not losing the settings for the PIDs. If not for this step the auto-tuning of the PID controllers must be done again, and the tuning might affect the sample.

3.8 Spec and DAWN

The measurements were acquired using the software spec and analyzed using the program Dawn Science.

3.8.1 Spec

Spec is a UNIX-based software package for instrument control and data acquisition. Developed by Certified Scientific Software(CSS) and first released in 1989. It now is widely used for X-ray diffraction [9]. In this experiment it was used to control the mechanical arm inside the X-ray box and measuring the X-ray diffraction.

3.8.2 DAWN

Data Analysis WorkbeNch(DAWN) is an opensource software built on the Eclipse/RCP platform to provide a visualization and analysis platform for data from any any synchrotron experiment[3]. Developed by Diamond Light Source (DLS), the European Synchrotron Radiation Facility (ESRF) and the European Molecular Biology Laboratory (EMBL, Grenoble) and first released in 2012.

Here DAWN was used to analyze the diffraction pattern measured through Spec. The program integrates over the diffraction pattern in azimuthal direction and gives the fitted intensity graph over q [20]. This data is then exported to a DAT-file. It is also used to create a curve fitting for the Pseudo-Voigt curve, (2.32), used to find the wavevector q_c, intensity and the Full Width at Half Maximum(FWHM). The data from every XRD image was reduced and exported to a DAT-file. Under this data reduction a calibration and the following corrections were done.

Calibration

In order to calibrate the measurements a calibration file must be created using a crystal with known diffraction pattern. Silver Behenate(AgBh) is used as a calibrant because of its clear and distinctive Bragg peaks[25]. The sample have to be placed in the exact same position as the clay samples. Because of this there has been made a tiny groove in on the extruding part of the copper plate. The AgBh is placed in a 1 mm glass capillary and brought into the groove. There the diffraction is measured and used as a reference by DAWN

Solid Angle Correction

Since the detector is flat with uniform square pixels, and we wish to measure the intensity over solid angles of a sphere. The projection of the detector pixels on the sphere gives a difference is solid angle per pixel. Where the solid angles further from incident ray cover a larger number of pixels[40]. This is corrected for using the solid angle correction.

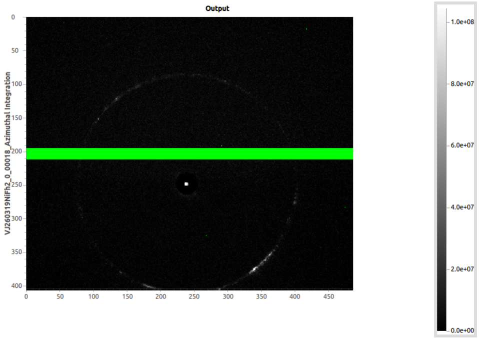

Figure 3.23: Mask placed on the gap between sensor modules and on five bad pixels.

Threshold Mask

Under processing of the information the threshold mask was implemented. This is used to remove any bad, overexposed or missing pixels from the raw data. These missing pixels are then corrected for in the azimuthal integration.

3.9 Experiments

The described setup was used to perform 3 experiments designed to demonstrate potential uses for this setup. The experiments were performed using Nickel Fluorhectorite. With chemical formula given by 2.1 with an x value of 0.5.

3.9.1 Experiment No. 1: CO_2 adsorption in NiFh with incrementally increasing pressure, on a long time scale.

Drying the sample under vacuum and heat, then bringing the temperature of the sample to 300 K. Continuously measuring the X-ray diffraction of the sample with the exposure time of 300 s, while the NiFh is exposed to CO_2 at incrementally increasing pressure. Beginning at 2 bars for 1 hour and increasing in steps of 2 bars to 6 bars. Spending 1 hour at every step. Then increasing in steps of 1 bar from 6 to 9 bars, still spending 1 hour at every step. Then increasing in smaller increments of 0.5 bars and spending 3 hours at every step from 9 to 15 bars before finally, while spending 3 hour at each step, increasing the pressure to 20 bars followed by 40 bars. This experiment was done to try to determine at which pressure the CO_2 intercalates in NiFh.

3.9.2 Experiment No. 2: CO_2 adsorption in NiFh with incrementally increasing pressure, on a short time scale.

Drying the sample under vacuum and heat, then bringing the temperature of the sample to 300K. Now as before continuously measuring the X-ray diffraction while exposing the NiFh to CO_2 at incrementally increasing pressure. Only now with a shorter exposure time 60 s and every step lasting 10 minutes (15 minutes after the first two steps). Here the pressure increases with 2 bars from 0 to 8 bars. Then with one bar up to 9 bars and from this point increasing with 0.5 bars up to 20 bars. This experiment was done to try to determine at which pressure the CO_2 intercalates in NiFh.

3.9.3 Experiment No. 3: CO_2 adsorption in NiFh at constant pressure and decreasing temperature, on a short time scale.

Drying the sample under vacuum, then bringing the temperature to 300 K and exposing it to CO_2 at 14 bars of pressure. Then measuring the X-ray diffraction continuously while lowering the temperature gradually, spending around 10 minutes at each step, until the Bragg peak moves considerably, indicating intercalation. After the peak moves the sample is then reheated until the CO_2 leaves the clay and the diffraction peaks return to its initial position. The pressure is then reduced to next step. Procedure is then repeated for 12, 10 and 8 bars. This experiment was performed to determine the temperature at which point the CO_2 intercalates in NiFh for a given pressure.

Chapter 4

Results

Here the results from the three experiments described in chapter 3 are presented. In addition to this the result of the calibration as well as some measurements illustrating the effective limits of the system and the drying procedure.

Every spectrum from an X-ray diffraction measurement is created through azimuthal integration of the X-diffraction image. This image were originally stored as a TIF-file as a grayscale image with values from 0 to 3227, and -1 for the gap between the detector modules and the broken pixels. Unless stated otherwise, the diffraction pictures presented have a display range between the values 0 and 15 and are converted into PNG-files before being imported to this document. The plots in the figures are created from DAT-files and text-files exported from DAWN and Labview, and are plotted using Python 3 and the plotting library matplotlib, except figure 4.30 and 4.31 which are drawn with TikZ. The intensity in the spectrum have an arbitrary unit over the scattering vector q. The temperature is given in Kelvin and the time is given in seconds(s), minutes(m) or hours(h) depending on the scale of the measurement series. The pressure is measured in a section which is cut of from the sample during changing of the pressure. So the pressure profiles does not represent the pressure on the sample, but in the section cut off from the sample during changing of the pressure. Every temperature measurement is off by 0.15 K since the temperature was measured originally in Celsius before 273 was added to convert it to Kelvin.

4.1 Calibration

The diffraction pattern from AgBh, used to calibrate the measurements, can be seen in figure 4.1. The two innermost rings were used in the calibration. The intensity spectrum can be seen in figure 4.2 and the diffraction rings can be seen in figure 4.3. Here the rings are labeled with the distances d, according to Bragg's law (2.25), between the repeating structure responsible for the corresponding diffraction peak. The sample was found to be 208.88 mm away from the detector. The calibration also gives us the maximum angle for the diffraction the detector is able to measure, $8.089°$ or 1.141173 Å^{-1}.

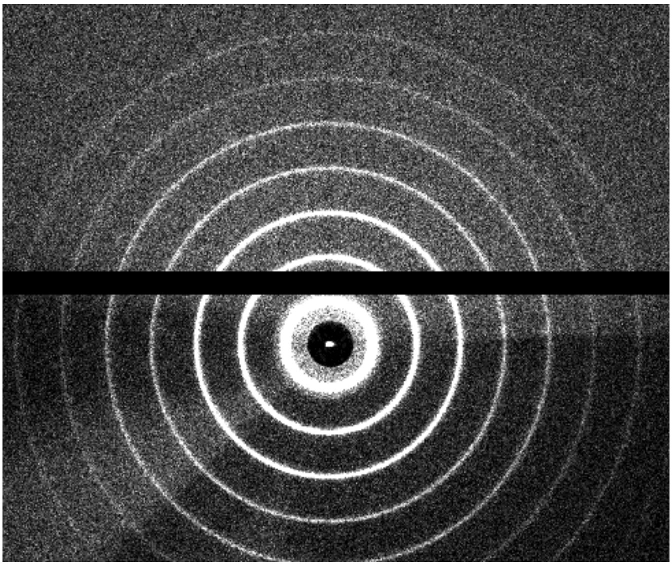

Figure 4.1: Diffraction rings for AgBh used for calibration of the X-ray measurements with the beam-stop in the middle. Image exposed for 20 minutes.

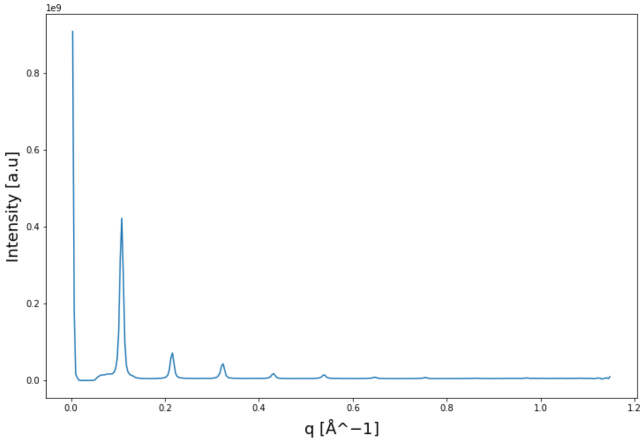

Figure 4.2: Entire XRD spectrum of AgBh through azimuthal integration of the diffraction pattern in figure 4.3. Here intensity of arbitrary units is shown against the scattering vector q from 0.0 to 1.1477 $Å^{-1}$.

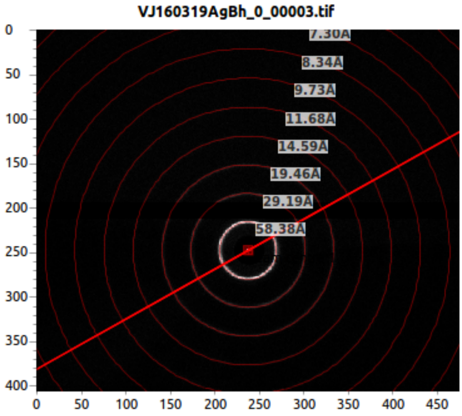

Figure 4.3: Her the diffraction rings from AgBh (figure 4.1) is shown with added markers with the distances d according to Bragg's law (2.25). Modified image originally created by DAWN.

4.2 Experiment No.1: CO_2 adsorption in NiFh at increasing pressure, on a long time scale

After drying the sample under vacuum at about 363 K, the sample is held at 300 K and exposed to CO_2 at increasing pressure. Each measurement has an acquisition time of 300 seconds and unless otherwise stated, the last measurement at each pressure step is presented in the figures 4.4,4.6, 4.7 and 4.8. The intensity for each XRD measurement is found through azimuthal integration, done by DAWN, and is presented in figure 4.4, with peak position, intensity and Full Width at Half Maximum(FWHM) as a function of pressure in figures 4.6,4.7 and 4.8 respectively. With added figures showing temperature (4.9, 4.10) and pressure profile (4.11) during the experiment.

Figure 4.4 shows the evolution of the 001-peak for NiFh as the pressure increases. The peak moved from q$_c$ $= 0.547$ Å^{-1} to q$_c$ $= 0.511$ Å^{-1}, when moving from vacuum to 39.5 bars of CO_2. Corresponding to moving from a d-spacing of 11.487 Å to 12.296 Å.
A composite image of the diffraction pattern for the NiFh at vacuum and 39.5 bars can be seen in figure 4.5. Where both the TIF-images have been added and the pixel values have been divided by two.

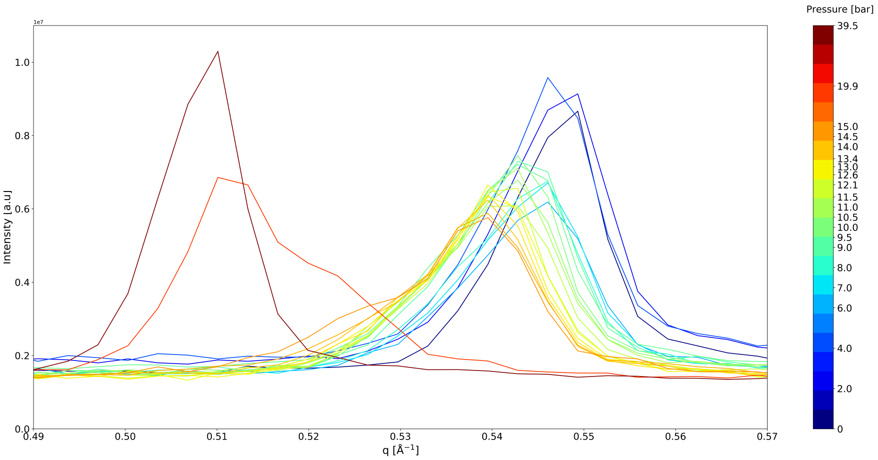

Figure 4.4: Bragg peak from NiFh, as it evolves with increasing pressure of CO_2 at a temperature of 300 K. Where the sample is held at each pressure for 1-3 hours. Where q_c moves from 0.547 $Å^{-1}$ at vacuum to 0.511 $Å^{-1}$ at 39.5 bar.

Peak position as a function of pressure can be found in figure 4.6, where the peak position is found through curve fitting using a pseudo-Voigt function, (2.32), using DAWN. Here the starting position of $q_c = 0.547$ $Å^{-1}$ at 0 bars and ending at $q_c = 0.511$ $Å^{-1}$.
The same fitting was used for the intensity and its FWHM as a function of pressure in figure 4.7 and 4.8 respectively. Here only the measurements from 12.0 to 39.5 bars is presented due to unreliable measurements of the value of the intensity due to loose kapton tape behind the sample.

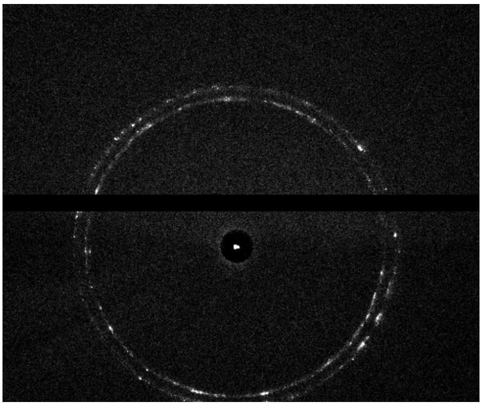

Figure 4.5: Composite image of NiFh at 0 bar and 39.5 bars of CO_2 pressure, outer and inner ring respectively.

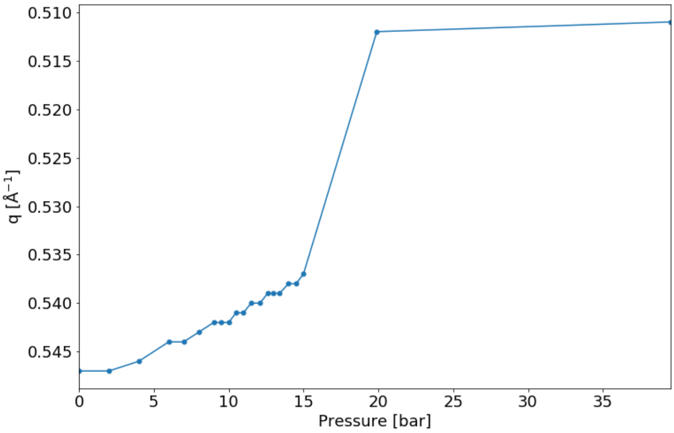

Figure 4.6: Wavevector q_c as a function of pressure. Starting at $q_c = 0.547$ at vacuum and ending at $q_c = 0.511$ at 39.5 bars.

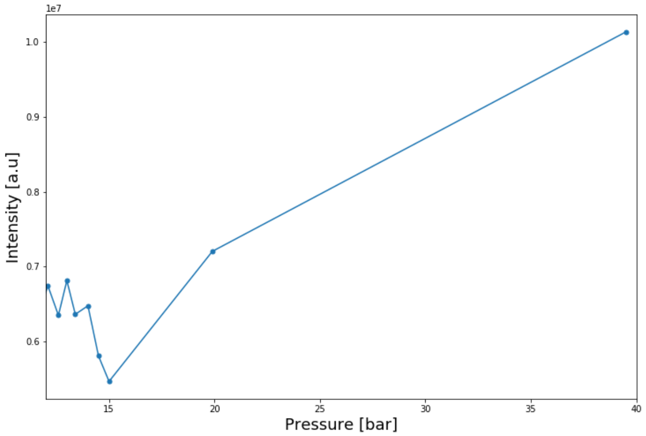

Figure 4.7: Intensity of the integrated image at the Bragg peak as a function of pressure. Starting at 12 bars due to unreliable intensity measurements for the earlier pressure levels.

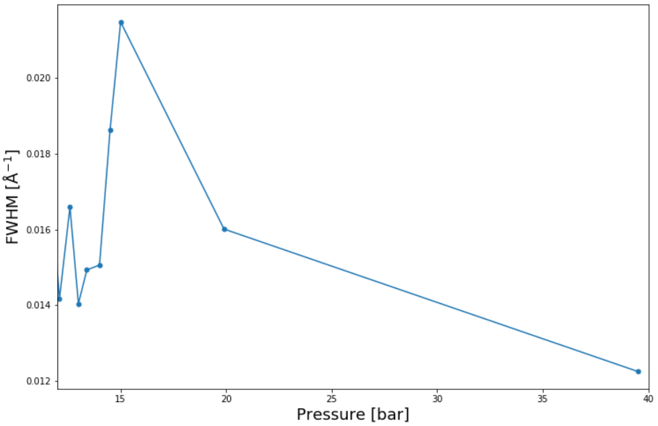

Figure 4.8: Full width at half maximum of the intensity curve at the Bragg peak from NiFh as a function of CO_2 pressure. From 12 to 39.5 bars of CO_2 pressure. Starting at 12 bars due to unreliable intensity measurements for the earlier pressure levels.

Temperature was measured during the entire experiment and the temperature profile can be seen in figure 4.9 and 4.10. The average temperature for the experiment was found to be 302.1 K, inside the copper plate and with a standard deviation of 0.1826 K. The thermocouple in contact with the copper plate was measured for 3 hours before it was moved. The average temperature on the copper plate was found to be 300.3 K with a standard deviation of 0.51 K.

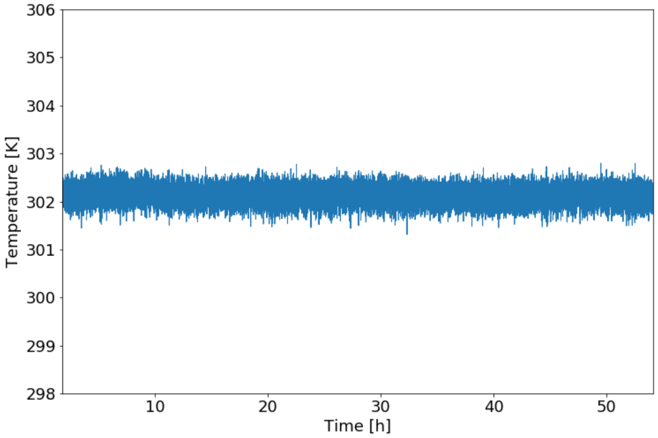

Figure 4.9: Temperature measurements during experiment No. 1. From thermocouple inside the metal plate. With the mean and standard deviation, μ =302.1 K, $\sigma = 0.1826$ K.

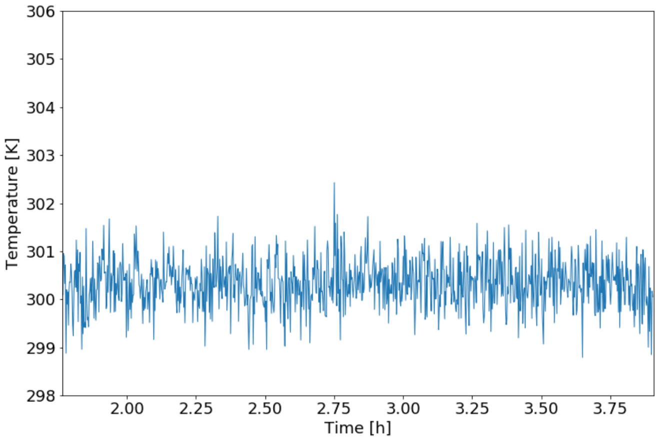

Figure 4.10: Temperature measurements during experiment No. 1. From thermocouple in contact with the same surface as the clay sample. Thermocouple was moved after 3 hours. The average temperature was measured to $\mu = 300.3$ K with a standard deviation of $\sigma = 0.51$ K

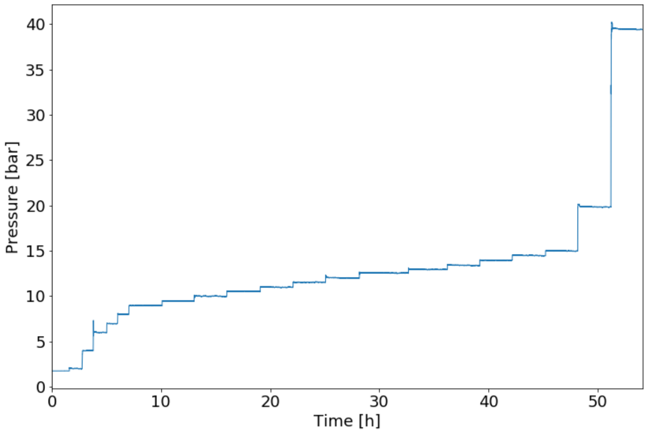

Figure 4.11: Pressure profile of sample during Experiment No. 1

4.3 Experiment No.2: CO_2 adsorption in NiFh at increasing pressure, on a short time scale

After drying the sample from experiment No.1 at vacuum and about 363 K, releasing captured CO_2 and absorbed water. The sample is held at 300 K and exposed to CO_2 at increasing pressure. The intensities is found through azimuthal integration and the peak position, intensity and FWHM is found using curve fitting to the pseudo-Voigt curve (2.32). All done with DAWN.

The evolution of the 001-Bragg peak is shown in figure 4.12. Where the sample was first held at the pressure stages 2.4 and 4.2 bar for 10 minutes. Here the diffraction intensity was measured over two images of 300 seconds each, but the intensity is divided by 5 so as to conform to the exposure time for the other measurements. Subsequent measurements were done with an exposure time of 60 seconds and the sample was held at each level for 15 minutes. The last measurement at each step is used in the figures. The peak position is found to move from $q_c = 0.547$ Å^{-1} to $q_c = 0.513$ Å^{-1} corresponding to a movement in d-spacing from 11.486 Å to 12.247 Å .

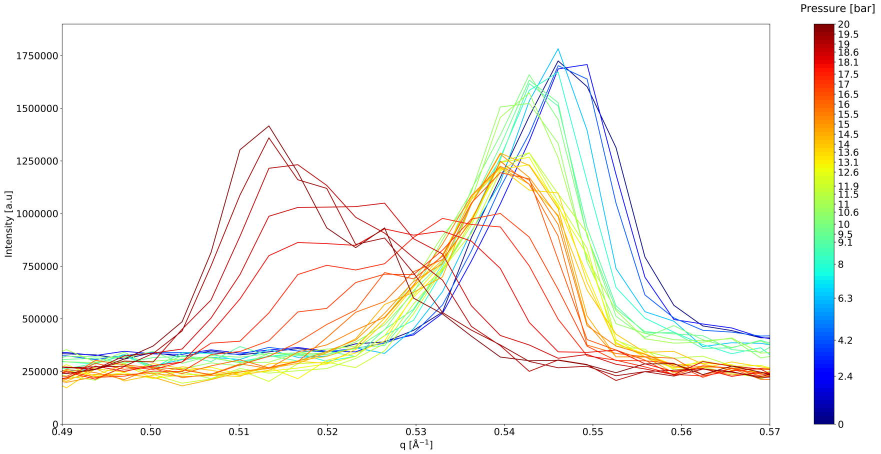

Figure 4.12: Bragg peak from NiFh, as it evolves with increasing pressure of CO_2 at a temperature of 300 K. Where the sample is held at each pressure for 10-15 minutes. Where q_c moves from 0.547 Å^{-1} at vacuum to 0.513 Å^{-1} at 20.0 bar.

Peak position as a function of pressure is found in 4.13.
With the intensity and its FWHM as functions of pressure is presented in figure 4.14 and 4.15 respectively. With the added figure 4.16 showing the pressure measurements.

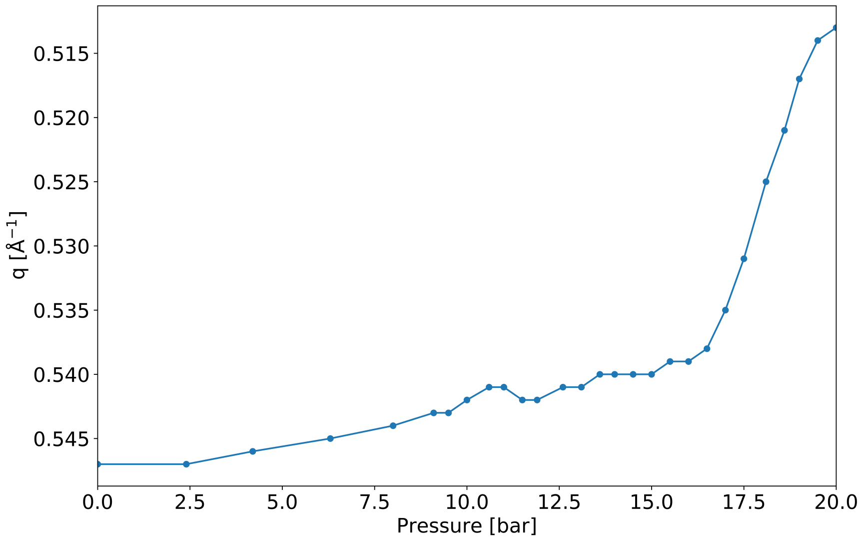

Figure 4.13: q position as function of pressure. Moving from $q_c = 0.547$ Å^{-1} to $q_c = 0.513$ Å^{-1}.

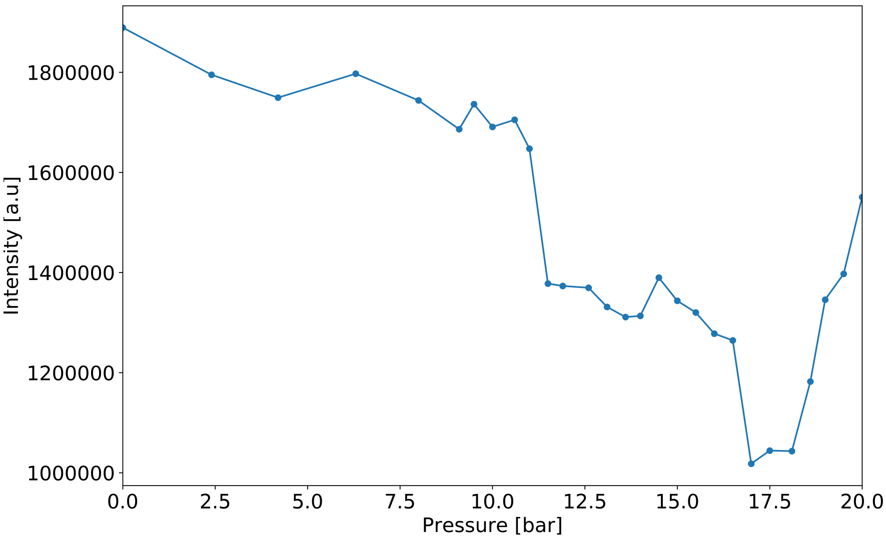

Figure 4.14: Intensity of the diffracted peak from the NiFh sample as a function of CO_2 pressure.

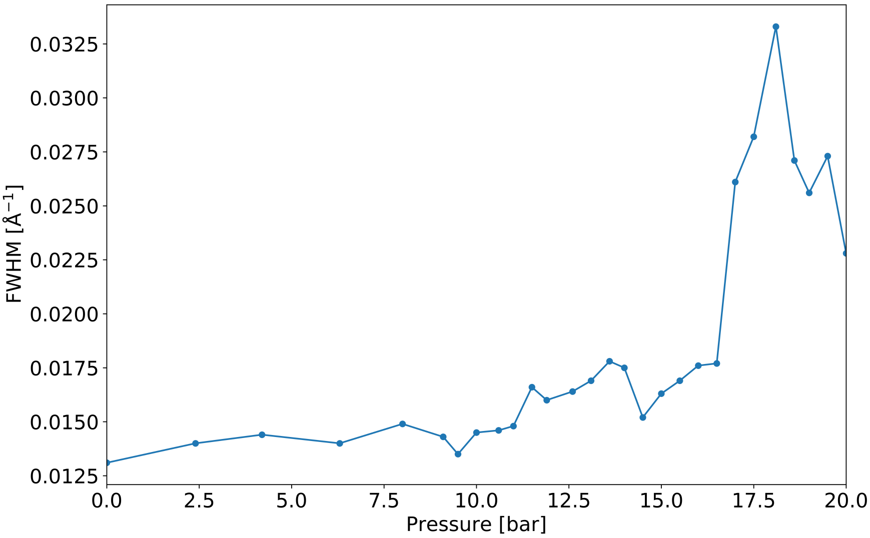

Figure 4.15: Full width at half maximum of the intensity curve at the Bragg peak from NiFh as a function of CO_2 pressure. From vacuum to 20.0 bars of CO_2.

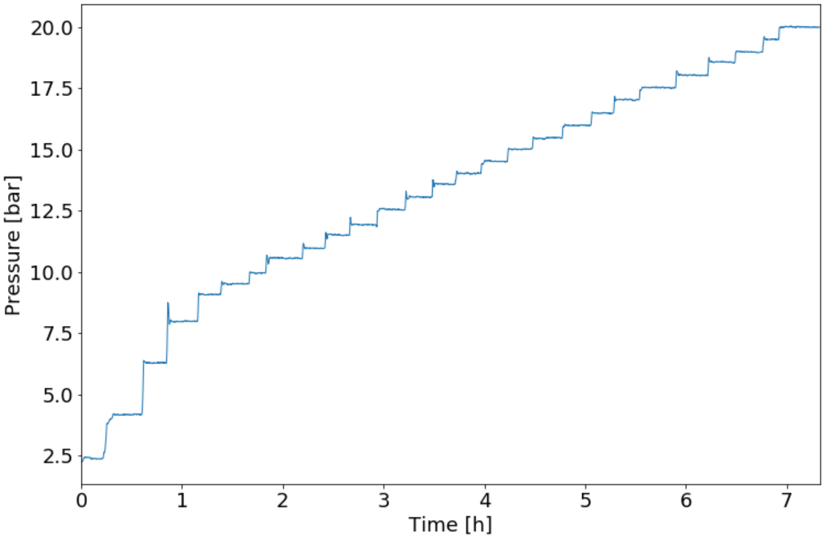

Figure 4.16: Pressure profile of experiment No. 2

4.4 Experiment No. 3: CO_2 adsorption in NiFh at constant pressure and decreasing temperature, on a short time scale.

After experiment No. 2 was completed the sample was reheated and the pressure lowered to 14 bar. When most of CO_2 was expelled from the sample. The sample was brought to 300 K and from there the temperature was slowly lowered until there was a noticeable shift in diffraction pattern. The diffraction was measured continuously, but only measurements with an average temperature 1 K lower than the former is included in the figure. In addition to this the last measurement in every series was also added. The average temperature is the average over the 60 seconds the diffraction image is formed. The pressure given is the average pressure under the measurement series. The change of the 001-peak position from 299.3 K to 291.9 K at 13.9 bar is shown in figure 4.17, with temperature profile in 4.18 with markers for the beginning of the measurement. The procedure of reheating and setting pressure was repeated for 14, 12, 10 and 8 bars.

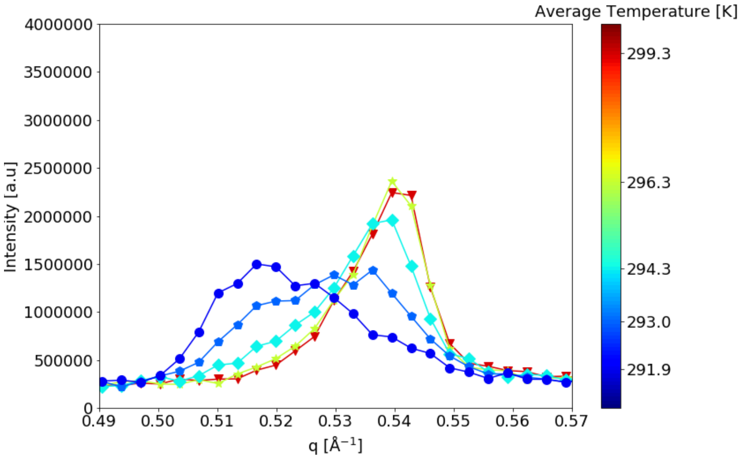

Figure 4.17: Intensity of the Bragg peak of NiFh exposed to 13.9 bars of CO_2. Each measurement is done at different temperature as indicated in the colorbar.

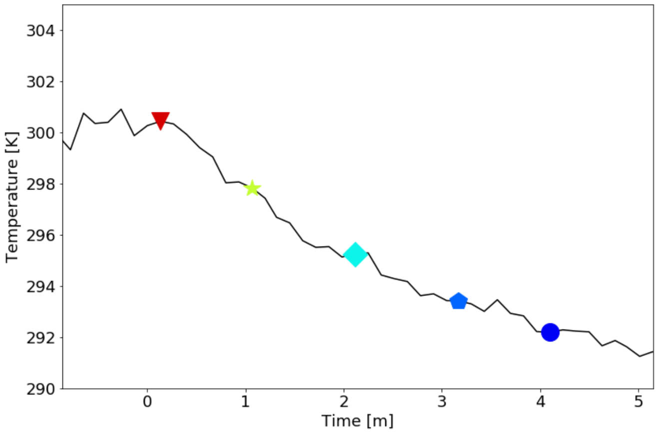

Figure 4.18: Temperature profile of the measurement series at 13.9 bars of CO_2 with added markers matching the measurements in 4.17 indicating the beginning of the measurement.

Change in 001-peak from 299.5 K to 296.0 K is shown in figure 4.19, with temperature profile in 4.20 with markers for the beginning of the measurement.

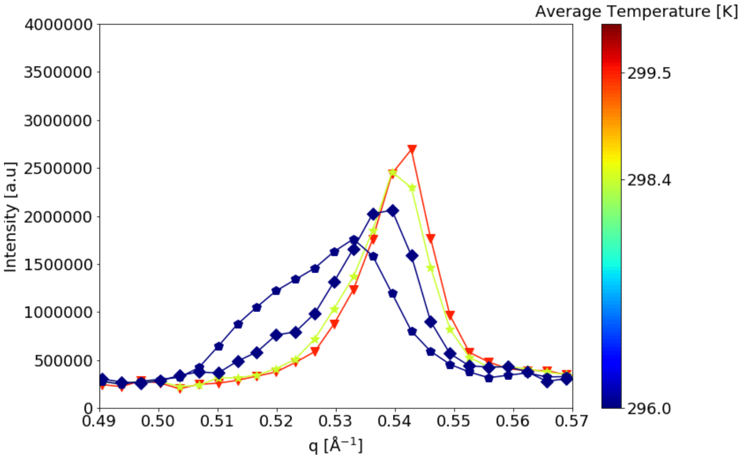

Figure 4.19: Intensity of the Bragg peak of NiFh exposed to 14.0 bars of CO_2. Each measurement, except the two last, are done at a different temperature.

Figure 4.21 for 12 bars with temperature profile in 4.22. Figure 4.23 and 4.24 for 10 bars and figure 4.25 and 4.26 for 8 bars. Each measurement has acquisition time of 60 seconds and the temperature is the average temperature of these 60 seconds.

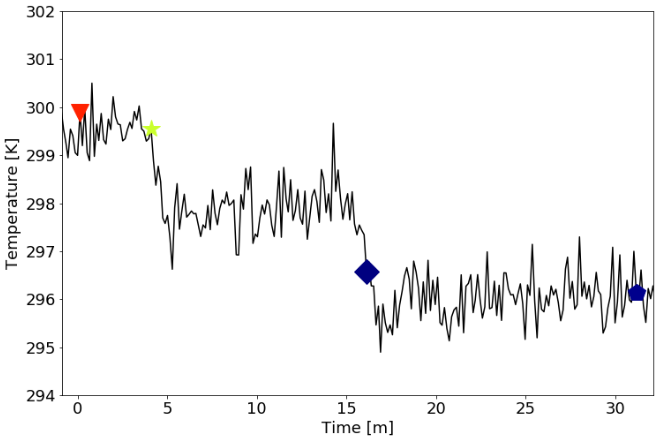

Figure 4.20: Temperature profile of the first measurement series at 14.0 bars of CO_2 with added markers matching the measurements in figure 4.19 indicating the beginning of the measurement.

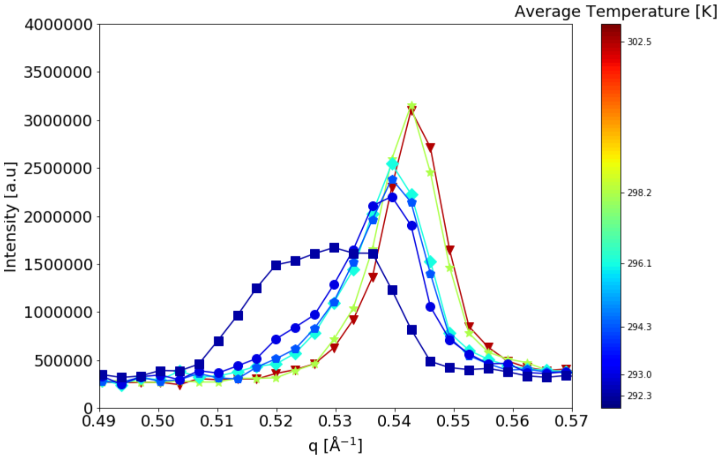

Figure 4.21: Intensity of the diffraction pattern of NiFh exposed to 12.0 bars of CO_2. Each measurement is done at different temperature as indicated in the colorbar.

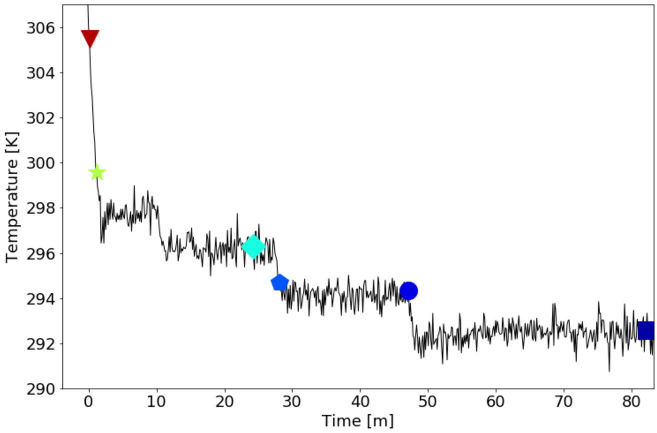

Figure 4.22: Temperature profile of the first measurement series at 12.0 bars of CO_2 with added markers matching the measurements in figure 4.21 indicating the beginning of the measurement.

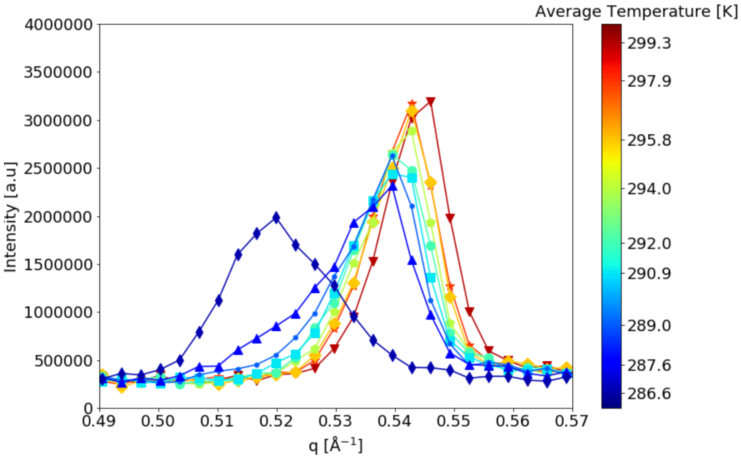

Figure 4.23: Intensity of the diffraction pattern of NiFh exposed to CO_2 at 10.0 bars of pressure. Each measurement at different temperature.

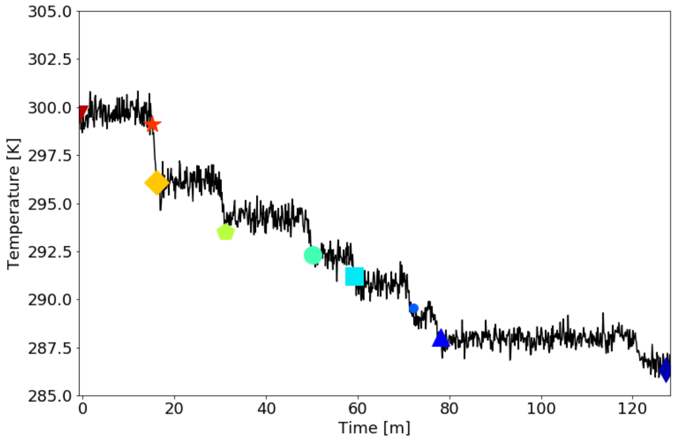

Figure 4.24: Temperature profile of the first measurement series at 10.0 bars with added markers matching the measurements in figure 4.23 indicating the beginning of the measurement.

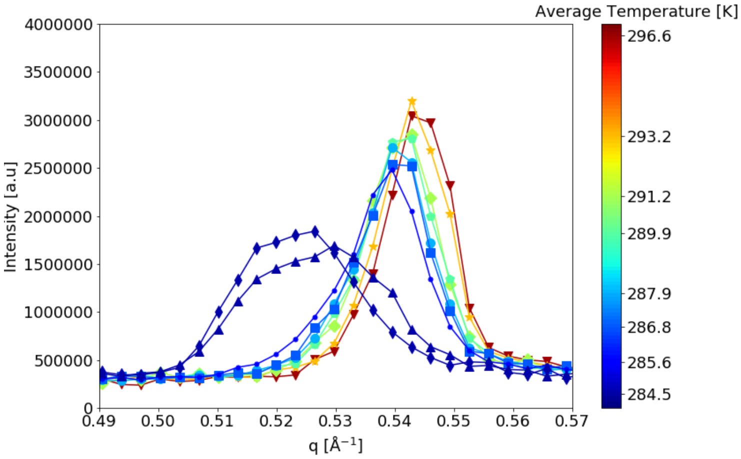

Figure 4.25: Intensity of the diffraction pattern of NiFh exposed to 8.0 bars of CO_2. Each measurement is done at different temperature as indicated in the colorbar.

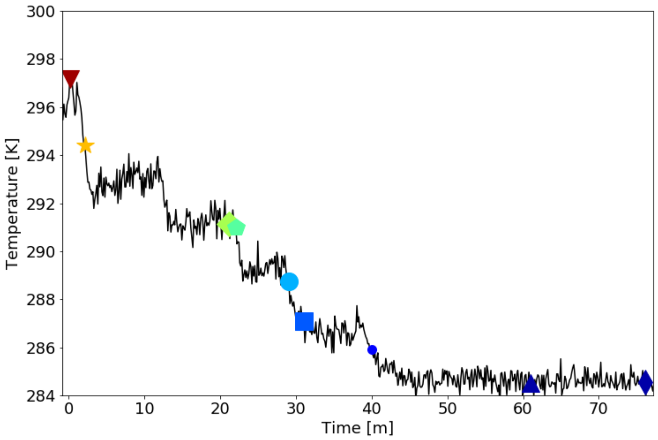

Figure 4.26: Temperature profile of the first measurement series at 10.0 bars with added markers matching the measurements in 4.23 indicating the beginning of the measurement.

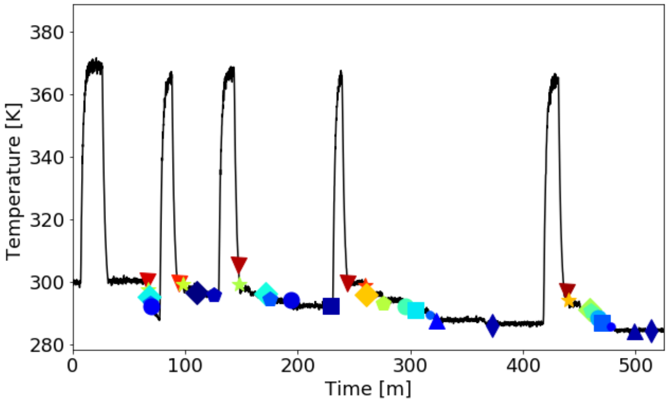

Figure 4.27: Temperature profile of experiment No. 3. With added markers for the measurements used in the figures 4.17, 4.19, 4.21, 4.23 and 4.25.

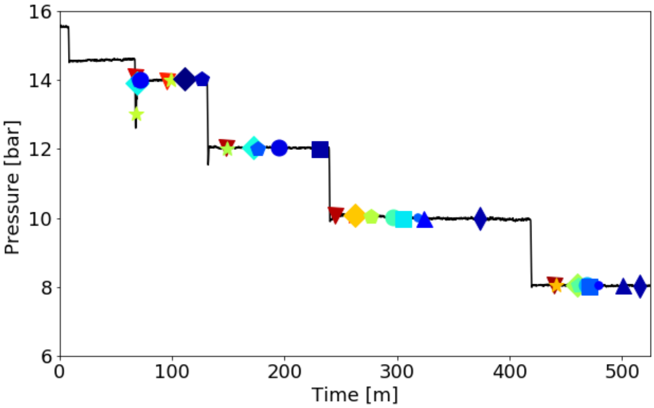

Figure 4.28: Pressure profile of experiment No. 3. With added markers for the measurements used in the figures 4.17, 4.19, 4.21, 4.23 and 4.25.

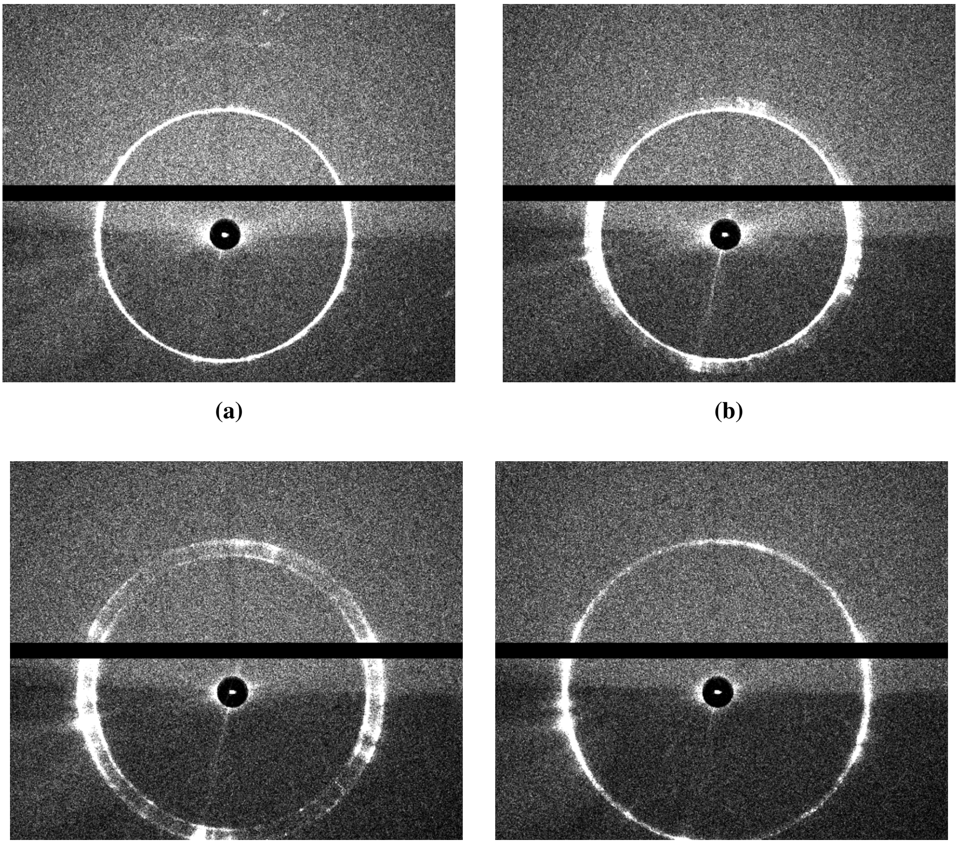

(a)

(b)

(c)

(d)

Figure 4.29: The diffraction pattern of NiFh at vacuum ($5.9 \cdot 10^{-2}$ mbar) before (4.29a), during(4.29b, 4.29c) and after drying (4.29d)

4.5 Drying

The samples were dried before they were exposed to carbon dioxide. Here is four diffraction images taken before, figure 4.29a, during, figure 4.29b 4.29c and after drying, figure 4.29d. With accompanying spectrum in figure 4.30 and temperature profile for the measurements in figure 4.31. The sample is measured with an exposure time of 20 minutes and taken in series.

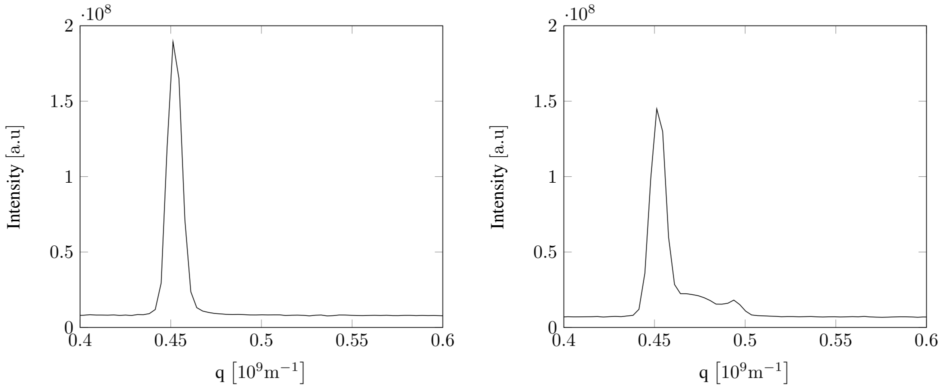

(a) Intensity of the (00l)-peak in hydrated NiFh. Here with a Bragg peak at $q_c = 0.4512$ Å^{-1} which corresponds to the distance $d = 13.924$ Å

(b) Intensity of the diffraction as the sample is drying. Measured during the first 20 minutes of drying.

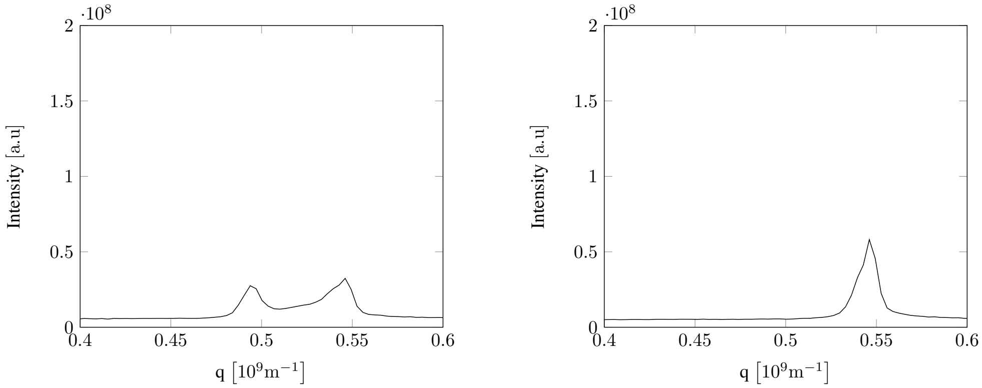

(c) Intensity of the (00l)-peaks. Measured after 20 minutes of drying. Peaks at $q_{c1} = 0.4905$ Å^{-1} and $q_{c2} = 0.5460$ Å^{-1}. Corresponding to a distance of $d_1 = 12.8101$ Å and $d_2 = 11.5061$ Å

(d) Intensity of (00l)-peak after drying. Peak is at $q_c = 0.54607076$ Å^{-1} corresponding to the interlayer distance of $d = 11.50617$ Å.

Figure 4.30: Intensity of diffracted X-ray from NiFh during the process of drying under vacuum.

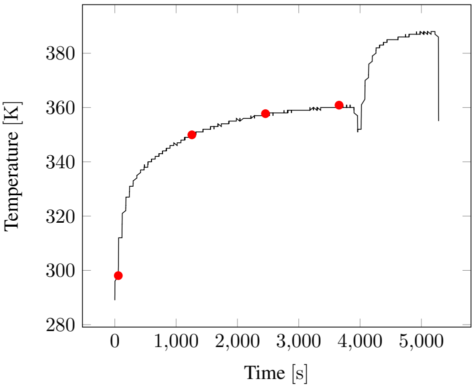

Figure 4.31: Temperate profile of the copper plate with added markers for the start of acquisition for diffraction image 4.29a, 4.29b, 4.29c and 4.29d.

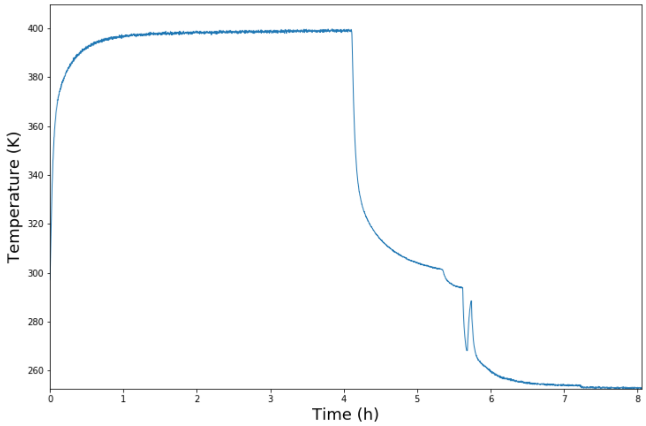

Figure 4.32: Temperature curve during heating. The average temperature from 1 h to 4 h was 398.3 K.

4.6 Limits of system

Here are two temperature measurements from two experiments where the sample was dried at max temperature and cooled to the minimum temperature. The temperature was measured inside the copper plate. The experiments ultimately failed due to gas leaks.

The heating can be shown in figure 4.32 were the maximum temperature was 399.7 K and the average from hour 1 to hour 4 was 398.3 K.
During the cooling, 4.33, the temperature was brought down to a minimum of 247.9 K and held the average temperature 248.5 the last hour from 1.9 h to 2.9 h.

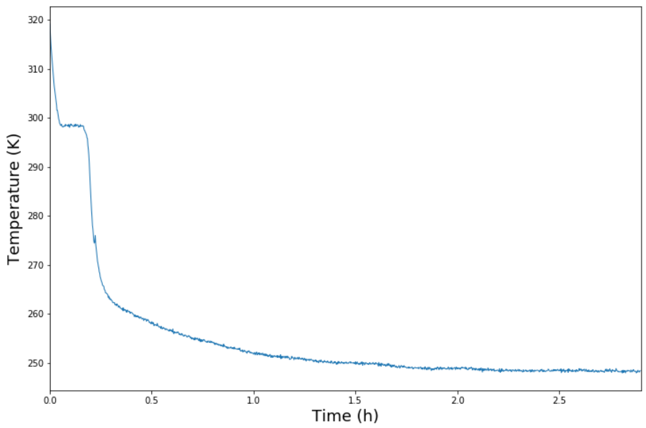

Figure 4.33: Temperature curve during cooling. From 1.9 h to 2.9 h the average temperature 248.5 K

Chapter 5

Discussion

5.1 Uncertainty

Ideally every sample should be placed at the same distance from the detector, but at the moment this is difficult for this setup. This results in a slight difference in sample to detector distance between samples. Which again affects the measured diffraction compared to the calibration image and to other samples. It is possible to correct for this using another known diffraction pattern. Here it would be natural to correct according to the known position for the dry 001-bragg peak of NiFh. Which has been measured to be at $q_c = 0.5511$ Å^{-1}, $d = 11.4012$ Å [2]. Adjust every q_c position by q_a giving the d,

$$d = \frac{2\pi}{q_c + q_a} \tag{5.1}$$

and the angle θ,

$$\theta = \sin^{-1}\left(\frac{\lambda(q_c + q_a)}{4\pi}\right) \tag{5.2}$$

The extruding part of the copper plate is 3 mm wide and the capillary containing the sample is 0.5 mm wide. If the capillary is off by ±1 mm this will have the following effect on the measured scattering vector.

If the sample is in correct position an the scattering vector is $q_c = 0.5511$ Å^{-1} then the angle between the incident and scattered X-ray is found through Braggs law,(2.25), to be 0.0676°. Then the q_c is placed 14.1418 mm from the beam center. This distance and the following are found through elementary geometry. If the clay sample is moved 1 mm away from the detector this gives the q_c position on the detector 14.2095 mm away from the beam center. Moving the sample 1 mm closer to the detector gives 14.0741 mm. Through linearity of the q_c values this gives an interval of 0.5537 to 0.5485 Å^{-1} in which the dry peak should be found. Giving an uncertainty of ±0.0026 Å^{-1}. Since there is a slight difference between the NiFh measured here and the NiFh used as a reference (x in

(2.1) is 0.5 here, while 0.6 in the measurement used as reference [2]) there is possible that this is the wrong approach to correcting the measurement.

5.2 Experiment No.1: CO_2 adsorption in NiFh at increasing pressure, on a long time scale

After drying the sample for an hour under constant vacuum of $5.9{\cdot}10^{-2}$ mbar at 363 K, the Bragg peak moved to the $q_c = 0.5493$ Å^{-1} position, within the uncertainty, and corresponding with $d = 11.439$ Å. After 20 more minutes there was no changes in the diffraction pattern. This is the maximum temperature when the circulator is running. The sample was deemed to be sufficiently dehydrated. When the sample was exposed to carbon dioxide at 2.0 and 4.0 bars. The peak moves slightly, as can be seen in figure 4.6, lowering the q value. This corresponds to a larger interlayer distance. The peaks width also increases. This is consistent with what to expect when clay first adsorbs CO_2. Some is taken up, but not enough to get a complete layer of carbon dioxide consistently between layers of the clay. Before the pressure was raised to 6.0 bars the plastic box was placed around the capillary. The box has a kapton covered window between the sample and the detector. This coincided with the sudden drop in intensity between 4.0 and 6.0 bars and is therefore the most probable explanation, since the peak does not appear to move. The kapton tape fell of sometime before the pressure stage of 12 bar. This makes the measurements of the intensity and FWHM unreliable and are therefore not included in the results.

The sample was held at each steps from 0 to 8 bars for one hour each. This is due to earlier more heuristic measurement, not included here, neither the peak or shape of the integrated curve was not expected to change a lot. Form figure 4.4, 4.6 it is clear that the peak moves, but very gradually.

This gradual movement of the peak continues nearly linearly, until the pressure was increased from 15 bars to 19.9. When the peak shifts by quite a lot. Suggesting intercalation of CO_2. Before this the peak had developed a slight shoulder at 11 bars increasing until it was quite pronounced at 15 bars. Indicating that the clay adsorbs carbon dioxide. This fits with the FWHM, figure 4.8, which grows from 13.5 bars to 15 bars and further for 20 bars, as well the intensity, figure 4.7, at the peak decreases for those same values. The peak does not move any further when increasing from 19.9 bars to 39.5, but the intensity increases and FWHM decreases, as more CO_2 intercalates.

It is not possible to determine the point at which the pressure is high enough to facilitate intercalation, but from the shoulder developing at 13-15 bar it seems reasonable to assume that it should be close to 15 bars. The temperature was approximately constant for the entire measurement series, while the pressure was controlled accurately over small steps.

5.3 Experiment No.2: CO_2 adsorption in NiFh at increasing pressure, on a short time scale

Here basically the same experiment was performed as in experiment No.1, but here over a much smaller time scale and several additional pressure levels. Since there is a temporal component to the intercalation this is not an ideal method to find the point at which the pressure is high enough for intercalation. It can however give an indication of what happens at different stages, and help planing further experiments.

The experiment starts at vacuum of $6.0 \cdot 10^{-3}$ mbar and peak position of $q_c = 0.547$ Å^{-1} and d-spacing of 11.487 Å. The first two pressure stages were held at 10 minutes. During the experiment it was determined that with this short amount of time it was difficult to analyze the diffraction images created, make sure that there wasn't a gas leak and increase the pressure to the next step correctly. Therefore the steps were increased to 15 minutes. As one can see, in figure 4.12, the peak moves steadily towards the left with the increasing pressure. With intensity lowering, 4.14, and and FWHM, figure 4.15 increasing. Both as expected when CO_2 is adsorbed. This trend continues until the intensity suddenly drops at 11.5 bars. At the same time the FWHM increases, but the peak position, figure 4.13, does not move noticeably. Form there the peak gradually moves towards the left and develops a shoulder and finally shifts at 16.5 bar. Where the q_c position suddenly moves with larger steps, the intensity goes down and the FWHM increases. This trend continues until 18 bars. Where the intensity at the peak increases and the width decreases. The peak moves further and seems to hit a plateau at 20 bar with $q_c = 0.513$ Å^{-1} corresponding to $d =$ 12.248 Å.

From these results the pressure point at which the CO_2 intercalates in NiFh is around 16.5 bar. There might also be something happening around 11.5 bar which could be worth investigating with a longer time frame as the adsorption can take some time (2.2). Which this experiment was not designed to take into account. We can also see that the system is capable of increasing pressure in small incremental steps.

Comparing the results from experiment 1 and 2 with other experiments conducted on NiFh the intercalation happens much faster than for NiFh with $x = 0.5$ than compared to $x = 0.6$ in (2.1). They also have different producers the NiFh tested here is produced by Josef Breu at Institut für Anorganische Chemie der Universität Regensburg(Institute for inorganic chemistry at Regensburg university)[7] while the other was produced by Corning Inc. Where with $x = 0.6$ the intercalation takes between 8 and 14 hours [34] at 253.15 K and 20 bars of CO_2, while here the intercalation happens almost instantaneously and and at much higher temperature and lower pressure.

5.4 Experiment No. 3: CO_2 adsorption in NiFh at constant pressure and decreasing temperature, on a short time scale.

This experiment is designed to use the temperature control to find at which temperature the carbon dioxide intercalates for different pressures. For the first test the temperature decreased too rapidly, as well as there being some irregularities with the pressure, as can be seen far to the left in figure 4.28. The results is still included as it gives an indication of how sensitive the intercalation is to temperature.

The sample is reheated under pressure, 14 bar, therefore the clay is not entirely free of CO_2 and the peak does not move to the dry position. The temperature is decreased slower than the previous measurement series. Here the peak moves at 296 K. After almost 20 minutes at that 296 K. This indicates at least that time does have factor in the intercalation and for a proper experiment the sample should spend more then 20 minutes at each step.

For 12 ,10 and 8 bars the same procedure was followed and the peak shifted at 292.3 K, 286.6 K and 285.6 K respectively. For a more accurate measurement the experiment must be done over a longer time perhaps an hour, or more at each step and starting with dry clay at vacuum. Even though these results are not particularly robust, they do give a starting point for further experiments and works as a proof of principle.

5.5 Drying

All of the above measurements have to a certain degree assumed that the samples were dry when the measurements began. I will therefore take a closer look at the drying process.

The Bragg peak from the one molecule water layer in NiFh should be at 0.457 $Å^{-1}$ [2] corresponding to an interlayer distance of 13.749 Å. This is not far of from the measured q= 0.451 $Å^{-1}$ and 13.924 Å and even closer when adjusting the peak according to the dry peak, giving a d-spacing of 13.779 Å. The During drying the peak shifts outwards and the diffraction ring becomes broader. This can be seen in figure 4.29c. In its spectrum, figure 4.30b, the peak has developed a shoulder on the right side. These on either side of the peak is usually a sign of transition from one state to another. After 20 minutes or so the broad circle is clearly separated into two circles 4.29c. This can also be seen in the spectrum in figure 4.30c. After 40 minutes of drying the 1 WL peak is gone and there is a peak at q= 0.5461 $Å^{-1}$ giving an interlayer distance of 11.5061 Å. This is 0.1048 Å away from the dry peak measured in [2]. The peak is still quite broad after 40 min. This indicates that there is could still be some water left in the sample. This could be removed with further drying, but there might be some complications in connection with prolonged drying as the epoxy adhesive is quite close to the heating source. Increasing the heat by adding another heating element is also an option, if the glue is heat resistant. However the heat should not go higher then 423 K since this might affect the charge density and swelling of the clay[41]. The heat might also contribute to the broadness of the peak due to the Debye-Waller factor, this should however disappear with lower temperature on the plate.

Another solution could be to dry the sample outside of the X-ray chamber using for example swagelok quickconnects, which allows us to dry the sample under vacuum and transfer them to the gas connection without much air entering the sample. These components were ordered but did not arrive in time for them to be tested.

5.6 Limitations

The X-ray home station has limitations connected to both the X-ray source and the detector. The relative low intensity of the beam makes it necessary to expose the detector for at least 1 minute to get an image with a good enough signal to noise ratio to be able to use. This means that any development that takes place over a shorter scale than 1 minute would not be possible to investigate.

The detector limits the measurements through the pixel, energy and temporal resolution. Due to the in-house detectors low angular resolution the peaks are only about 10-16 pixels broad. This gives some uncertainty to the measurements and makes it necessary to use curve fitting in order to properly characterize the peaks. The detector also has a maximal count rate of $2{\cdot}10^6$ X-ray/sec for each pixel, the dynamic range of 20 bits, able to show values from 0 to 1048575, and a frame rate of 20 Hz.

Experiments requiring a higher resolution than what the home laboratory is able to provide can be done at a synchrotron. Here the intensity is up to 1000 times higher and emitted in pulses of nano seconds enabling time resolved studies. Larger detectors allow for greater angular resolution as well as a wider range of angles possible to investigate.

It is hard to measure the temperature of the sample correctly. Even tough we measure the temperature at the surface which the capillary is in contact with, this is not a guarantee the the clay inside the capillary has the same temperature. More on this in the Further Development section.

During cooling the humidity inside the X-ray chamber will cause ice to form on the copper and eventually either on the capillary or in the way of the X-rays obstructing the diffraction image. Two viable solutions to this was tried. The first was taping shut as much as possible of the holes to the chamber and before closing it placing a large container with silica gel inside the chamber bringing the humidity down to about 5%. This works for a couple of hours, before the humidity rises again and it becomes necessary to add more silica gel. The other solution can be preformed in parallel with the silica gel and is adding a small N_2 stream along the capillary. This also keeps ice from forming on the capillary, but has the downside of raising the temperature by a couple of degrees.

Depending on the position of the arm inside the X-ray chamber one of the heating element

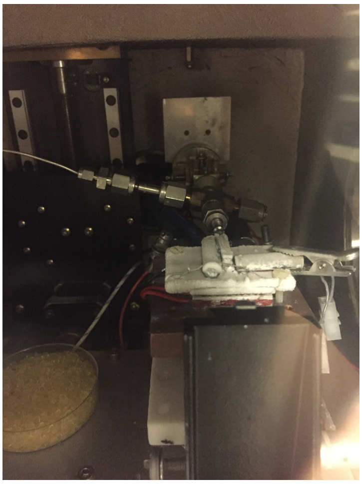

Figure 5.1: Frost developing on the plate and covering the sample capillary.

may be in the way of the Debye Scherrer cone from the clay, this is currently prevented by removing the heating element behind the extruding part of the copper plate. This could easily be avoided if the extruding part was a little higher, or the groove, in which the heating element is placed, was deeper. In the images in figure 4.29 the lower half of the images is clearly darker then the upper half. This can be explained by that the air scattering is blocked by the platform copper plate. The impact of this on the measured intensity is minimal for shorter lengths, but can be noticeable for longer exposure times with a weakly scattering sample. This can be corrected for by subtracting the background by measuring without a sample and the platform at the same position. This could be hard to do since the platform is manually controlled, but should be possible.

5.6.1 Sample cell

Compared to earlier experiments there were a noticeable increase in gas leaks. These earlier experiments were preformed with the same procedure for sealing the capillaries to the gas system as in the experiment described here. The two most likely explanations for this is that the epoxy glue was not properly mixed, or that because the capillaries were shortened the glue is much closer to the heat source and the heat weakened the glue. The last explanation seems the most likely since I was not the only person with this problem. The strength of the glue drops to about 15% of its original strength at 353 K. This can problem can be mitigated by using longer capillaries. This in turn means that the sample holder must be moved further inside the X-ray chamber. There is room for this but this might limit the movement of the arm inside the X-ray chamber. Moving the sample cell further inside the X-ray chamber also makes it possible to use whole capillaries instead of shortened ones. This will make it possible to change from glass to quartz capillaries and make the burst pressure/pressure rating of the system higher. This goes for whole capillaries in general.

Other sample cells used for in-situ XRD measurements are often a a open ended glass, quartz or sapphire capillary fastened in both ends with the possibility of a gas flow through the system [5, 10, 28]. These sample cells are capable of doing experiments up to 100 bars for quartz [28] and 300 for sapphire. Which is sufficient for studying adsorption of super-critical CO_2 which enters this state at about 304 K and 73 bar [6]. At super-critical state CO_2 can be adsorbed at even higher temperatures and pressures more relevant for petroleum reservoirs and geological CO_2 sequestration conditions[32]. It is possible to adapt the system to this kind of sample cell by placing the cylinder containing the clay on the copper plate.

5.7 Further development

The sample cell and method used in the experiments works well, but could still be developed further. As mentioned the sample holder can be moved further inside the X-ray chamber to allow for a larger distance between the heat source and the glue and some pressure test to determine the burst pressure of the cell.

For more efficient heating a third heating element could be placed on the copper plate. In addition to this a metal clamp could be placed over the elements leading more of the radiating heat into the copper plate.

The setup reached its desired cooling temperature and could probably be made to reach even lower temperatures if so desired. This could be done using a more efficient circulation cooler and/or a third Peltier-element in the peltier stack. As is it is not possible to add a third element, due to lack of space between copper plate and the glass capillary held perpendicular by the goniometer head.

The system currently requires wires to be the connected and disconnected when moving from cooling to heating and vice versa. This makes room for human flaw and takes more time learning to use it. This can be resolved either through the use of a third power supply. One for heating, a second for measuring and a third for cooling. A simpler solution would be to use an electronic switch for controlling the current passing through the either the heating-elements or the Peltier-elements. The pressure control and valves could also be automated, but an electronic valve was unavailable and too expensive given the project funds. The pressure pump can be automated making increasing or lowering the pressure possible without supervision. This among others will make it easier doing measurements over a long time scale.

Several alterations could be done to the Labview code. First of all some of the functions/squares could be made into VI modules for a more streamlined code. This will make it easier to modify later if the need arises.

As is, the temperate control works well and is able to keep a sample at a given temperature between 253 K and 399 K for longer periods of time. To study the intercalation dependency on temperature it would be useful to be able to create a temperature ramp function. This is currently possible to do manually within the range of approximately -268 to 398 K. Where the circulator alone is responsible for the cooling. The Peltier-elements have different output at certain temperature which does not scale linearly and can therefore not be reliably controlled over a range of temperatures. This can be remedied through a gain-schedule. Through a gain-schedule a non-linear system can be broken into several intervals where the system can be approximately controlled through different linear controllers. Each with a different PID-gains.

The system is currently measuring temperature two ways. First through a thermocouple inside the extruding part of the copper plate, and the second through a thermocouple in contact with the surface of the extruding part of the copper plate. The latter must be manually placed in contact with the plate and has a tendency to move when the plastic box is placed above. This creates an uncertainty in the measurement. There is also the fact that we wish to measure the temperature inside the capillary. A solution to this would be to do a measurement both inside the copper plate and inside a glass capillary in contact with the copper. Then create a mapping function for the entire range of temperatures the system can produce. With a detector with a wider range of angles NaCl could be used as a reference. Where the Bragg peaks dependence on temperature is known [39]. It might also be possible to place a thin thermocouple inside the glass capillary, entering the closed end of the T-connection the sample is mounted on, and measure temperature in-situ. With the variable length of the capillary this is hard to do consistently. Another argument for moving the sample holder further away from the copper plate.

Chapter 6

Conclusion

The experiments indicates that CO_2 intercalates at around 16.5 bar for NiFh at 300 K. In addition to this we have preliminary results that CO_2 intercalates at 296.0 K, 292.3K, 286.6 K and 285.6 K for 14 bar, 12 bar, 10 bar and 8 bar respectively.

While none of the experiments gave any conclusive results, they do however show that the designed setup is capable of keeping the sample at constant temperature between 253 and 398 K while doing long term XRD measurements. It is also able to control the pressure within the sample with a high degree of accuracy. Making it possible to preform experiments with incremental pressure steps. The same goes for incremental temperature steps. While currently not covering the entire temperature range it should be possible to do from 268 K to 399 K. However due to a high occurrence of gas leaks from the sample cell it is recommended that the sample holder is placed further away from the heated copper plate.

Bibliography

[1] J. Als-Nielsen. Elements of modern x-ray physics, 2011.

[2] M. Altoé, L. Michels, E. dos Santos, R. Droppa, G. Grassi, L. Ribeiro, K. Knudsen, H. Bordallo, J. Fossum, and G. da Silva. Continuous water adsorption states promoted by ni2+ confined in a synthetic smectite. *Applied Clay Science*, 123: 83 – 91, 2016. ISSN 0169-1317. doi: https://doi.org/10.1016/j.clay.2016.01.012. URL `http://www.sciencedirect.com/science/article/pii/S0169131716300138`.

[3] M. Basham, J. Filik, M. T. Wharmby, P. C. Y. Chang, B. El Kassaby, M. Gerring, J. Aishima, K. Levik, B. C. A. Pulford, I. Sikharulidze, D. Sneddon, M. Webber, S. S. Dhesi, F. Maccherozzi, O. Svensson, S. Brockhauser, G. Náray, and A. W. Ashton. *Data Analysis WorkbeNch* (*DAWN*). *Journal of Synchrotron Radiation*, 22(3):853–858, May 2015. doi: 10.1107/S1600577515002283. URL `https://doi.org/10.1107/S1600577515002283`.

[4] Berkeley Earth. Global temperature report for 2018, 2018.

[5] U. Bösenberg, C. Pistidda, M. Tolkiehn, N. Busch, I. Saldan, K. Suarez-Alcantara, A. Arendarska, T. Klassen, and M. Dornheim. Characterization of metal hydrides by in-situ XRD. *International Journal of Hydrogen Energy*, 39(18):9899–9903, 2014. ISSN 03603199. doi: 10.1016/j.ijhydene.2014.02.068.

[6] G. M. Bowers and J. S. H. D. W. B. S. D. W. E. D. K. R. J. Schaef, H. Todd; Loring. Role of cations in co 2 adsorption, dynamics, and hydration in smectite clays under in situ supercritical co 2 conditions. *Journal of Physical Chemistry. C*, 121(1), 2017. ISSN 1932-7447.

[7] J. Breu, W. Seidl, A. Stoll, K. Lange, and T. Probst. Charge homogeneity in synthetic fluorohectorite. *Chemistry of Materials*, 13(11):4213–4220, 2001. ISSN 08974756.

[8] A. Busch, P. Bertier, Y. Gensterblum, G. Rother, C. Spiers, M. Zhang, and H. Wentinck. On sorption and swelling of co 2 in clays. *Geomechanics and Geophysics for Geo-Energy and Geo-Resources*, 2(2):111–130, 2016. ISSN 2363-8419.

[9] Certified Scientific Software. *spec ™X-Ray Diffraction Software: X-Ray Diffraction SoftwareUSER MANUAL and TUTORIALS, REFERENCE MANUAL, STANDARD MACROS GUIDE, FOUR-CIRCLE REFERENCE, ADMINISTRATOR'S GUIDE, HARDWARE REFERENCE*, 2017.

[10] H. Cheng, C. Lu, J. Liu, Y. Yan, X. Han, H. Jin, Y. Wang, Y. Liu, and C. Wu. Synchrotron radiation x-ray powder diffraction techniques applied in hydrogen storage materials - a review. *Progress in Natural Science: Materials International*, 27(1): 66–73, 2017. ISSN 1002-0071.

[11] M. Chidambaram. Relay tuning of pid controllers : For unstable mimo processes, 2018.

[12] G. J. Da Silva, J. O. Fossum, E. Dimasi, K. J. Måløy, and S. B. Lutnaes. Synchrotron x-ray scattering studies of water intercalation in a layered synthetic silicate. *Physical review. E, Statistical, nonlinear, and soft matter physics*, 66(1 Pt 1), 2002. ISSN 1539-3755.

[13] Dectris. *User Manual PILATUS3*, 2019.

[14] Dectris. *Technical Specifications and Operating Procedure PILATUS3 R 200K-A Detector System*, 2019.

[15] i. Encyclopedia Britannica. Peltier element. In *Encyclopedia Britannica*. Fall 2014 ed. edition, 1998. URL `https://www.britannica.com/science/Peltier-effect`.

[16] i. Encyclopedia Britannica. Seebeck effect. In *Encyclopedia Britannica*. Fall 2014 ed. edition, 1998. URL `https://www.britannica.com/science/Seebeck-effect`.

[17] i. Encyclopedia Britannica. X-ray. In *Encyclopedia Britannica*. Spring 2010 ed. edition, 2010. URL `https://www.britannica.com/science/X-ray`.

[18] i. Encyclopedia Britannica. Clay mineral. In *Encyclopedia Britannica*. Fall 2014 ed. edition, 2014. URL `https://www.britannica.com/science/clay-mineral#ref618498`.

[19] B. K. G. T. G. L. B. K. G. T. F. Bergaya and G. Lagaly. *Handbook of Clay Science*, volume 1 of *Developments in Clay Science Ser.* Elsevier Science & Technology, 1 edition, 5 2006. ISBN 9780080457635.

[20] J. Filik, A. W. Ashton, P. C. Y. Chang, P. A. Chater, S. J. Day, M. Drakopoulos, M. W. Gerring, M. L. Hart, O. V. Magdysyuk, S. Michalik, A. Smith, C. C. Tang, N. J. Terrill, M. T. Wharmby, and H. Wilhelm. Processing two-dimensional x-ray diffraction and small-angle scattering data in dawn 2. *Journal of Applied Crystallography*, 50 (3):959–966, 2017. ISSN 1600-5767.

[21] Z. R. M. A. E. d. S. C. d. F. R. D. J. A. G.-S. J. F. G. Grassi, L. Michels and G. da Silva. Cation exchange dynamics confined in a synthetic clay mineral. *Eur. Phys. J. Special Topics*, (223):1883–1893, 6 2014.

[22] P. Giesting, S. Guggenheim, A. van Groos, and A. Busch. X-ray diffraction study of k- and ca-exchanged montmorillonites in co sub 2 atmospheres. *Environmental Science & Technology*, 46(10), 2012. ISSN 0013936X. URL `http://search.proquest.com/docview/1016012286/`.

[23] G. Grassi, L. Michels, Z. Rozynek, M. A. S. Altoé, E. C. dos Santos, C. L. S. da Fonseca, R. Droppa, A. Gholamipour-Shirazi, J. O. Fossum, and G. J. da Silva. Cation exchange dynamics confined in a synthetic clay mineral. *The European Physical Journal Special Topics*, 223(9):1883–1893, Sep 2014. ISSN 1951-6401. doi: 10.1140/epjst/e2014-02233-8. URL `https://doi.org/10.1140/epjst/e2014-02233-8`.

[24] D. M. F. E. L. H. Henrik Hemmen, Erlend G. Rolseth, J. O. Fossum, and T. S. Plivelic. X-ray studies of carbon dioxide intercalation in na-fluorohectorite clay at near-ambient conditions. *Langmuir*, (28):1678–1682, 2012. URL `https://www.nature.com/articles/s41598-018-30283-2.pdf`.

[25] T. Huang, H. Toraya, T. Blanton, and Y. Wu. X-ray-powder diffraction analysis of silver behenate, a possible low-angle diffraction standard. *Journal Of Applied Crystallography*, 26:180–184, 1993. ISSN 0021-8898.

[26] Hydrargyrum. File:bragg_diffraction_2.svgg, 2011. URL `https://commons.wikimedia.org/wiki/File:Bragg_diffraction_2.svg`.

[27] IPCC. Global warming of 1.5 °c : an ipcc special report on the impacts of global warming of 1.5 °c above pre-industrial levels and related global greenhouse gas emission pathways, in the context of strengthening the global response to the threat of climate change, sustainable development, and efforts to eradicate poverty, 2018.

[28] T. R. Jensen, T. K. Nielsen, Y. Filinchuk, J. E. Jrgensen, Y. Cerenius, E. M. Gray, and C. J. Webb. Versatile in situ powder X-ray diffraction cells for solid-gas investigations. *Journal of Applied Crystallography*, 43(6):1456–1463, 2010. ISSN 00218898. doi: 10.1107/S0021889810038148.

[29] C. Kittel. Introduction to solid state physics, 2005.

[30] J. E. K. D. K. J. O. F. Leide P. Cavalcanti, Georgios N. Kalantzopoulo2. A nanosilicate material with exceptional capacity for co2 capture and storage at room temperature. *Scientific Reports*, (6), 8 2018. URL `https://www.nature.com/articles/s41598-018-30283-2.pdf`.

[31] LinguisticDemographer. File:tubesectrum.jpg, 2006. URL `https://commons.wikimedia.org/wiki/File:TubeSpectrum.jpg#/media/File:TubeSpectrum.jpg`.

[32] N. Loganathan, G. Bowers, A. Yazaydin, H. Schaef, J. Loring, A. Kalinichev, and R. Kirkpatrick. Clay swelling in dry supercritical carbon dioxide: Effects of interlayer cations on the structure, dynamics, and energetics of co 2 intercalation probed by xrd, nmr, and gcmd simulations. *Journal of Physical Chemistry C*, 122(8):4391–4402, 2018. ISSN 19327447.

[33] L. Michels. *Intercalation Phenomena of Carbon Dioxide, Water or Ions in Smectite Clay*. PhD thesis, Norwegian University of Science and Technology, Høgskoleringen 1, 12 2015.

[34] L. Michels, J. O. Fossum, Z. Rozynek, H. Hemmen, K. Rustenberg, P. A. Sobas, G. N. Kalantzopoulos, K. D. Knudsen, M. Janek, T. S. Plivelic, and G. J. D. Silva. Intercalation and retention of carbon dioxide in a smectite clay promoted by interlayer cations. *Scientific Reports*, 5(1), 2015. ISSN 2045-2322.

[35] F. Mo and B. Tøtdal. *Forelesningsnotater i Røntgenkrystallografi*. Inst. for Fysikk NTH, 1994.

[36] E. Myshakin, V. Romanov, and R. Cygan. Natural materials for carbon capture. Technical report, 11 2010.

[37] National Instruments. What is labview, 2019. URL `http://www.ni.com/en-no/shop/labview.html`.

[38] T. P. Whorf, M. Wahlen, R. B. Bacastow, S. C Piper, C. D. Keeling, M. Heimann, and H. A. Meijer. Atmospheric co2 and 13co2 exchange with the terrestrial biosphere and oceans from 1978 to 2000: Observations and carbon cycle implications. In *A History of Atmospheric CO*, volume 177 of *Ecological Studies*, pages 83–113. Springer New York, New York, NY, 2005. ISBN 9780387220697.

[39] P. D. Pathak and N. G. Vasavada. Thermal expansion of NaCl, KCl and CsBr by X-ray diffraction and the law of corresponding states. *Acta Crystallographica Section A*, 26(6):655–658, Nov 1970. doi: 10.1107/S0567739470001602. URL `https://doi.org/10.1107/S0567739470001602`.

[40] B. R. Pauw. Everything saxs:small-angle scattering pattern collection and correction. *Journal of physics. Condensed matter : an Institute of Physics journal*, 26(23), 2014. ISSN 1361-648X.

[41] J. P. Quirk and B. K. G. Theng. Effect of surface density of charge on the physical swelling of lithium montmorillonite. *Nature*, 187(4741), 1960. ISSN 0028-0836.

[42] E. Rubin. Summary of the ipcc special report on carbon dioxide capture and storage, 2018.

[43] J. Thomas, B. Bohor, and R. Frost. Surface area measurements on clays. *Clays and Clay Minerals*, 18(6):405–407, 1970. ISSN 0009-8604.

[44] A. Trepte. Image:montmorillonit.svg, 2007. URL `https://commons.wikimedia.org/wiki/File:Montmorillonite-en.svg`.

[45] A. Urquizo. File:pid_en.svg, 2011. URL `https://commons.wikimedia.org/wiki/File:PID_en.svg`.

[46] Wiso. File:ewald_sphere.svg, 2009. URL `https://commons.wikimedia.org/wiki/File:Ewald_Sphere.svg`.

[47] Xenocs. *GeniX- Installation and Operational Manual*, 2007.

Appendix A

Appendix

Code used in the analysis of the measurement data.

```
def find_measurment(f): #Find where measurements start in a long file.
    a=[]
    for line in f:

        if line == '\n':
            print("found an end of line")
            print(line)
            print(line+1)
            a.append(f)
    return a

def qtod(q): #convert from wavevector to interlayer distance
    d=[]
    for i in q:
        d.append((2*np.pi)/i)

    return d

def datafromfile(measurement_file): #read take in file and returns data
    times=[]
    timestamp=[]
    pressure=[]
    temperature0=[]
    temperature1=[]
    posision=[]
    measurment_pos=[]
    measurment_number=0
    for i in f:

        try:
            if i != '\n'and i!="Time  Temperature Pressure\n":
                a=datetime.strptime(i[0:19],"%d.%m.%Y %H:%M:%S")
                timestamp.append(a)
                #b=i[:18]
                b=float(i[20:30].replace(',','.'))
```

```
                temperature0.append(b)
                #print(b)
                c=float(i[31:39].replace(',','.'))
                pressure.append(c)
                d=float(i[40:].replace(',','.'))
                d=d+273

                temperature1.append(d)
                measurment_number=measurment_number+1
            if i=="Time  Temperature Pressure\n":
                measurment_pos.append(measurment_number)
        except ValueError:
                print(i)
                print(measurment_number)

    t0=time.mktime(timestamp[0].timetuple())
    for i in (timestamp):  # Converts timestamps into seconds from
                           #start of measurement.
        noe=time.mktime(i.timetuple())-t0
        times.append(noe)
    return timestamp,times,pressure,temperature0,temperature1



def timestamp_from_folder(file): #extracts timestamps and names of tif files
#from file created from the comand "ls -lc >timestamp.txt"
    timestamp=[]
    filename=[]
    for i in file:
        i=i.replace("\n", "");
        if len(i)>42:
            tempstring= i[34:36]+ i[30:33]+"2019"+i[37:42]+":00"

            if i.endswith("tif"):
                timestamp.append((datetime.strptime(tempstring,"%d%b%Y%H:%M:%S")))
                filename.append(i[43:])
    return filename,timestamp

def sum_tif_images(filename,a,b,tif_path): #adds tif-images from
                           #number a to number b in the series.
    sumdat = np.empty([407,487])
    length=b-a
    for i in range(length):
        im=Image.open(tif_path+filename[i])
        imdat = np.array(im)
        sumdat = sumdat + imdat

    #Scaling intensity
    scale_ar = (1/length)*(sumdat)
    scaleim= Image.fromarray(scale_ar)
    tempname="sum_images" +filename[a][0:10]\
    +filename[a][16:20] + "-" +filename[b][16:20]
    scaleim.save(tempname+'.tif')
    name=tempname+'.tif'
    return name

def add_tif_images(filename1,filename2,tif_path): #adds two tif-images
```

```
    sumdat = np.empty([407,487])

    im=Image.open(tif_path+filename1)
    imdat = np.array(im)
    sumdat = sumdat + imdat
    im=Image.open(tif_path+filename2)
    imdat = np.array(im)
    sumdat = sumdat + imdat

    scale_ar = (1/2)*(sumdat)
    scaleim= Image.fromarray(scale_ar)
    tempname="sum_images" +filename1[0:10] +filename1[16:20] + "-" +filename2[16:20]
    name=tempname+'.tif'
    scaleim.save(name)
    return name



def time_position(tif_timestamp,acquisition_time,measurement_timestamp):
    #gives time position of start and end of a acquisition
    #matching the time measured with labview

    b=bisect_left(measurement_timestamp, tif_timestamp)
    a=bisect_left(measurement_timestamp,\
    tif_timestamp-timedelta(seconds=acquisition_time))
    return a, b #returns position in measurment file.
                # from beginning to end of the measurment.

class image:
    def __init__(self, name ,name_dat,timestamp,a_time,
    measurementfile,Iq_file,dat_path,tif_path):
        self.name = name
        self.timestamp=timestamp
        self.a_time=a_time*(b-a)
        data=datafromfile(measurementfile)
        self.a,self.b=time_position(timestamp,a_time,data[0])
        self.temp0=data[3][self.a:self.b]
        self.pres=data[2][self.a:self.b]
        self.I,self.q=I_q_from_dat(datfile,dat_path)




def dat_filenames(filenames):
    #takes in the tif-files names and gives out a list of the
    #dat. files conected to them
    names_dat=[]
    for i in filenames:
        names_dat.append(i[0:-4]+"_00000.dat")
    return names_dat
#def add_images(image):

def I_q_from_dat(dat_file,dat_path):#takes in dat file and returns I and q
    q=[]
    I=[]
    with open(dat_path+dat_file) as tsv:
        for line in csv.reader(tsv, delimiter="\t"):
```

```
        #a=float(i[20:30].replace(',','.'))
            a=float(line[0])
            q.append(a)
            b=float(line[1])
            I.append(b)
    return I,q
```